Numerical model of Ni-infiltrated porous anode solid oxide fuel cells

by

Eric Freddy Hardjo

A thesis submitted to the
Department of Chemical Engineering
in conformity with the requirements for
the degree of Master of Applied Science

Queen's University
Kingston, Ontario, Canada
June 2012

Abstract

A numerical model for solid oxide fuel cells with Ni-infiltrated porous anode has been described. The novel contribution of the work is the development of a semi-continuous film model to describe the infiltrated Ni-phase. This model relates experimentally controllable parameters, namely, Ni- loading, porosity and pore size to the effective electronic conductivity of the Ni-phase and the number of active reaction sites or the triple phase boundary (TPB). The semi-continuous film model was incorporated in a two-dimensional (2D) SOFC model. The 2D model considers the coupled gas-phase transport, charge transport and electrochemical kinetics to directly examine the effect of Ni loading and porosity on the electrochemical performance of Ni-infiltrated SOFC anodes. From the semi-continuous film model, an optimal Ni loading that corresponds to a maximum in TPB length was identified. Comparison of effective electronic conductivity and TPB length for a Ni-infiltrated anode with those for a composite Ni-YSZ anode suggests that an infiltrated Ni anode with adequate electrical conductivity and sufficiently high TPB length can be fabricated even at a very low Ni loading. Comparison of various porous anodes with varying Ni loading, it was determined that maximum electrochemical performance does indeed correspond to anode with maximum TPB length. It was also determined that an infiltrated anode will have higher performance capabilities when compared to the conventional composite electrodes. However, degradation of performance may result due to degradation of connectivity in the infiltrated Ni. The methodology to model the latter effect was also proposed.

Co-authorship Statement

I hereby declare that I am the sole author of this thesis. Dr. Dayadeep Monder and my supervisor, Dr. Kunal Karan provided valuable technical input and editorial feedback and are co-authors of the two manuscripts presented in this thesis.

Acknowledgments

I wish to express my sincere gratitude to my supervisor, Dr. Kunal Karan for his invaluable guidance, strong encouragement, financial support and for reminding me of the big picture when I get lost in the details of my work. I would also like to express my deepest gratitude to my mentor and good friend, Dr. Dayadeep Monder for his guidance in this project, his tremendous patience in the numerous problem-solving sessions as well as helping me develop my appreciation of great Canadian beer.

I wish to express my appreciation and gratitude to Dr. Viola Birss, Dr. Scott Paulson and Ms Parastoo Keyvanfar from University of Calgary and Dr. Amir Hanifi and Mr. Alireza Torabi from University of Alberta, for their help and patience in developing my understanding in the experimental characterization of the Ni-infiltrated SOFC anodes. I would also like to acknowledge the NSERC Solid Oxide Fuel Cell Canada Strategic Research Network for funding support.

I wish to thank the past and present students and researchers at the Queens-RMC Fuel Cell Research Centre for fostering a conducive working environment. In particular, I would like to thank Barath, Duncan, Hae-Won for all the technical discussions on porous media transport and fundamental electrochemistry. I would also like to thank my elder Jedi, Jeff, for all the brainstorming, debugging sessions and valuable feedback. A special thanks to my housemates in Kingston for giving me a home away from home: Adam, my bros at the bromansion (Niels, Nicky and Jordan), Tom and Chantal. The incredible meals and fun

times at each home will definitely be missed. I would also like to thank my friends from Dupuis and Queen's for all their encouragement and support: Jonas, Eric, Jen, Calista, Phil, Kevin, Ian, Dan, Erin, Bernard and Karim.

I wish to extend my deepest gratitude to my family, especially my parents and my brother for their continuous and strong support throughout my undergraduate and graduate degrees.

Last but not least, I thank my significant other and soon-to-be wife, Ya Mei, for her infinite amount of patience and unconditional love this past 10 years. Your encouragement to keep pushing forward helped sustained my drive and passion for this thesis.

"There are two things you need in life: knowledge and trust. Trust in yourself and trust in others."

- Soehardjo The

Table of Contents

List of Tables

List of Figures

Nomenclature

A_{des}	Pre-exponential factor for the hydrogen desorption reaction from Nickel
A_{film}	Surface area of 2D film
A_{film}^{c}	Surface area corresponding to the percolation threshold
A_{sub}	Available surface area of substrate
$\tilde{D}_{ij}$	Multicomponent Fick diffusivity
D_i^K	Knudsen diffusion coefficient
D_{ij}	Binary diffusion coefficients
d_{pore}	Pore diameter
e_{ed}^-	Electron within the Nickel
E_{des}	Activation energy for the hydrogen desorption reaction from Nickel
F	Faraday's constant
f_{pack}	Packing factor of lattice
$H_2O_{ads,el}$	Absorbed water molecule on YSZ surface
$H_{ads,ed}$	Adsorbed hydrogen molecule on the Nickel surface
h_{cap}	Height of spherical cap
i_{H2}^*	Exchange current factor for anodic current density
$i_{0,H2}$	Exchange current density for hydrogen oxidation
$i_{0,O2}$	Exchange current density for oxygen reduction
i_{tar}	Target current density
i_v	Distributed volumetric current density

$\mathbf{j}_i$	Mass diffusive flux
K_n	Knudsen number
k_π	Proportionality constant relating P_π to p and p_c
k_{cond}	Conductivity proportionality constant
k_{thick}	Thickness proportionality constant
ℓ_{ed-el}	Contact perimeter between the electrolyte particles and the electrode particles
ℓ_{peri}	Perimeter length of the percolated film
$O_o^x(ads, el)$	Lattice oxygen on YSZ
L	length of the continuous film element
M_i	Molecular weight of species i
n_π	Number of film particles that make up the percolated network
n_{ed}	Number fraction of the electrode
N	Total number of substrate particles
$O^{2-}_{ads,el}$	Oxygen ion absorbed on YSZ surface
$O_{ads,ed}(c)$	Absorbed oxygen molecule on the cathode surface site
$OH^-_{ads,el}$	Hydroxide ion absorbed on YSZ surface
p	Site occupation
p_c	Critical site occupation
p_g	Total gas pressure
P_π	Probability that an occupied site belongs to the percolated network
P_{ed}	Probability of the electrode particles to form a percolated network of its own phase from the dense electrolyte to the current collector
P_{el}	Probability of the electrolyte particles to form a percolated network of its own phase from the dense electrolyte to the current collector
p_{ref}	Reference site occupation
$R_{a,c}$	Reaction term with R_a representing the anode reaction term and R_c representing the cathode reaction term

R_{cap}	Radius of spherical cap
R_{film}	Bulk resistance of film
R_{sint}	Radius of sintered substrate particle
r_{sint}	Radius of sintered film particle
R_{unsint}	Radius of unsintered substrate particle
$s_{ads,ed}(a)$	Empty Nickel site
$s_{ads,ed}(c)$	Empty LSM site
$s_{ads,el}$	Empty YSZ site
t_c	Thickness of film that corresponds to the film's critical volume fraction
t_{film}	Film thickness
t_{ref}	Reference film thickness corresponding to p_{ref}
U_{fuel}	Fuel utilization
$\mathbf{v}$	Velocity vector for the gas mixture
$V_o^{\cdot\cdot}(ads, el)$	Oxygen vacancy on YSZ
$V_{air,inlet}$	Mean inlet air velocity
V_{film}^c	Film volume fraction for which there is a presence of percolated film clusters
$V_{fuel,inlet}$	Mean inlet fuel velocity
x_{H2O}^b	Mole fraction of H_2O in the bulk region
x_{H2}^b	Mole fraction of H_2 in the bulk region
x_{H2O}^r	Mole fraction of H_2O at the reaction sites
x_{H2}^r	Mole fraction of H_2 at the reaction sites
x_j	Mole fraction of species j
y_{H2}^{in}	Amount of H_2 (in mols) that needs to be fed to the anode
y_{fuel}	Amount of fuel (in mols) that will be consumed with the target current density
Z_{ed-el}	Average coordination number between the electrode and electrolyte particles

Z_{film}	Coordination number of film particles
Z_{sub}	Coordination number of substrate particles

Greek letters

$\alpha_{a,c}$	Charge transfer coefficient
$\Delta\phi_{eq}$	Equilibrium phase potential
η_{act}	Local activation overpotental
ϵ_a	Reactant activation barrier
ϵ_c	Product activation barrier
η^a_{conc}	Anode concentration overpotential
Γ	Surface site density of Nickel
γ_0	Sticking coefficient of absorption of hydrogen gas onto Nickel
κ	Permeability of the gas
λ^m_{ij}	Mean free path length of a molecule in a gas mixture
λ_{ij}	Mean free path length of species i in species j
λ_{TPB}	Triple phase boundary length
μ_g	Viscosity of gases
μ_{mix}	Averaged viscosity for gas mixture
$\Omega^{2,2}_i(T^*)$	Collision integral expressed as a function of reduced temperature
ω_i	Mass fraction of species i
ϕ_{ed}	Electrode phase potential
ϕ_{el}	Electrolyte phase potential
ϕ^v_{ed}	Electrode solid phase volume fraction
ϕ^v_e	Electrolyte solid phase volume fraction
ϕ_g	Pore phase porosity
ρ	Density of the gas mixture
ρ_i	Density of species i

ρ_{film}	Film resistivity
σ_{α}^{comp}	Effective conductivities of the composite electrode and electrolyte
$\sigma_{ed(i)}^{eff}$	Effective electrode conductivity
$\sigma_{el(i)}^{eff}$	Effective electrolyte conductivity
σ_{eff}^{infil}	Effective conductivity of infiltrated Ni film
σ_i	Collision diameter for gaseous species
σ_{ij}	Averaged collision diameter of the species i in a gas mixture of species i and j
θ_c	Fractional free LSM surface sites
$\theta_O(c)$	Fractional surface coverage of the adsorbed oxygen molecule on the LSM surface
θ_{film}	Contact angle of film particles
θ_{H2O}	Fractional surface coverage of the water molecule on the YSZ surface
θ_{Ni}	Fractional free Nickel surface sites
θ_{OH}	Fractional surface coverage of the adsorbed hydroxide ion on the YSZ surface
θ_O	Fractional surface coverage of the oxide ion on the YSZ surface
θ_{sub}	Contact angle of substrate particles
θ_{YSZ}	Fractional free YSZ surface sites
τ	Perimeter sites: Number of sites that neighbour occupied sites in the percolated clusters
τ_s	Surface tortuosity

Chapter 1

Introduction

With the world driven by industrialization and technology, we are consuming more energy to sustain a technologically advanced lifestyle, and as a result, exhausting the Earth's limited fossil fuels supply. There is an increasing need for the research and development of sustainable energy technologies that can sustain current industrial growth and reduce our dependency on fossil fuels. Fuel cells are one of the many sustainable technologies that are currently being advanced to displace the current power generation capabilities of thermal plants for electric generation and internal combustion engines.

1.1 Fuel cells

Fuel cells are electrochemical devices that convert the chemical energy of the fuel directly into electricity. A fuel cell is made up of three key components: an anode where oxidation of the fuel takes place, a cathode where reduction of oxygen occurs and an electrolyte that selectively transports ions from one electrode to the other. Fuel cells can be categorized by the type of electrolyte that is used. Currently, significant effort is being directed towards the development of polymer electrolyte-based fuel cells, molten carbonate electrolyte-based cells and ceramic fuel cells (Petric, 1999). This thesis focuses on the ceramic fuel cells.

1.1.1 Solid oxide fuel cells

Ceramic fuel cells are more commonly known as solid oxide fuel cells (SOFC) because they utilize an electrolyte that is a solid oxide. SOFCs are high temperature fuel cells that operates over a temperature range of 500^oC - 800^oC. When SOFCs are operational, they co-generate electricity and recoverable heat energy at combined electrical and thermal efficiencies of more than 85% (Singhal and Kendall, 2003). Figure 1.1 is a schematic diagram of the workings of an SOFC at cell level with a magnified detailed schematic depicting the reaction sites of the SOFC, more commonly known as the triple phase boundary (TPB). It is the boundary where the three phases, electronic phase, ionic phase and gas phase meet and this is the site where the power generating electrochemical reactions occur (Zhu and Kee, 2008). Air enters the cathode where oxygen is subsequently reduced to oxide ions

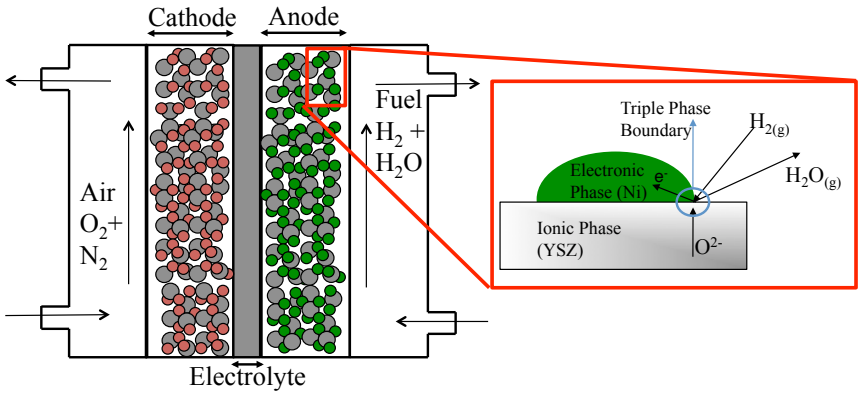

Figure 1.1: Schematic diagram of a SOFC at a cell level. The triple phase boundary concept is introduced with the zoomed-in schematic.

that are transported across to the anode via the ceramic electrolyte. The global oxygen reduction reaction is expressed in Equation [1.1]

$$\frac{1}{2}O_2(g) + 2e^- \leftrightharpoons O^{2-} \tag{1.1}$$

The dense ceramic electrolyte is an oxygen ion conductor that is impermeable to gas and has negligible electronic conductivity. The fuel enters the anode and is electrochemically

oxidized, generating electrons and producing heat at the same time. The fuel can be pure hydrogen or hydrogen-containing reformate. For hydrogen fuel, the chemical byproduct of the reaction is simply water. If a hydrogen-containing reformate is used, carbon dioxide is formed at the anode in addition to water. The electrons produced by the oxidation of the fuel, flows through an external circuit to the cathode where they are used to convert oxygen to oxide ions. The potential difference between the anode and cathode times the current produced generates electrical power. The global fuel (H_2) oxidation reaction is expressed in Equation [1.2]

$$H_2(g) + O^{2-} \leftrightharpoons H_2O(g) + 2e- \tag{1.2}$$

The most common material used for the dense electrolyte is Yittria-stablizied Zirconia (YSZ). YSZ has been identified as the best electrolyte at present owing to its good stability under reducing atmospheres, negligible electronic conductivity, and acceptable oxygen ion conductivity for 800^0C. One of the most common SOFC cathodes is Strontium-doped Lanthanum Manganite (LSM) YSZ composite. The LSM perovskite has been verified to have excellent chemical stability and high oxidation resistance at high temperatures while providing acceptable cathode performance. Conventional solid oxide fuel cell anodes consist of sintered Nickel (Ni) and YSZ particles forming a percolating network between the dense electrolyte and the current collector. The Ni metal acts an electrocatalyst for the fuel while providing electron conductivity. The YSZ particles in the composite anode and cathode cermet provide ion conductivity, have acceptable thermal expansion compatibility and mechanical stability as well as providing high porosity and surface area for the electrode structure for effective mass transport of the gas-phase species (Singhal and Kendall, 2003). In this thesis, my focus is on the SOFC anode, specifically, an anode-supported SOFC design.

1.1.2 Conventional composite anode

Anode-supported SOFCs have been identified as a promising cell design for operation at lower temperatures because of low ohmic resistance contribution from the thin dense electrolyte and a thick anode layer that provides mechanical support for the cell without compromising transport of the gas phase species (Jiang, 2006). The limiting current of SOFC composite Ni-YSZ anode is closely related to the microstructural properties that dictate its effective transport properties. The spatial distribution and connectivity of each constituent phase influences the amount of active TPB present as well as the effective transport properties (electronic/ionic conductivity and gas-phase diffusivity). Each phase must be connected from the TPB to the source of the transported species in order for a section of TPB to be active. Specifically, there must be a connected electron conduction path through the Ni to the current collector, an oxygen ion conduction path through the dense electrolyte to the TPB, and a gas diffusion path from the fuel channel in an anode to the TPB. An increase in active TPB length has been linked to reduced polarization of the electrode for a given choice of electrode material, making increasing the amount of active TPB length in an electrode a key factor in an electrode optimization process (Tanner *et al.*, 1997). Characterization of the Ni-YSZ microstructural properties and correlating to the effective electronic, ionic conductivities and active TPB lengths is, therefore, necessary for the optimization of the electrode (Lee *et al.*, 2002).

Characterization of composite SOFC electrodes

In the preceding section, the important role of correlating electrode microstructure with effective electrode transport properties as well as directly linking electrochemical performance to the effective electrode transport properties and the distribution of active TPB was discussed. Designing high performance anodes or simulating the performance of anodes require

a quantitative relation between structure and property and between property and performance. Wilson *et al.* (2006) have developed focused ion beam-scanning electron microscope (FIB-SEM) techniques to reconstruct a three-dimensional images of composite electrodes as well as investigate the influence of material composition and pore volume on the electrode microstructure and ultimately relate the electrode microstructure to electrode performance. The three-dimensional image reconstruction experiments yield important quantitative information about the relationship between microstructural parameters of the electrodes to effective transport properties and active TPB lengths (Wilson and Barnett, 2008). At our Fuel Cell Research Centre, Professor Pharoah's group has developed several numerical reconstruction models of porous electrodes (Berson *et al.*, 2011). The measurement of effective transport properties of the electronic and ionic phase as well as the active TPB length allows for the detailed understanding how the microstructure parameters affect the anode performance.

There have been a wide variety of models that have been developed that estimate how the composite Ni-YSZ electrode microstructure influences its effective transport properties. The widely-adopted percolation and coordination-number theory has been used to describe the Ni-YSZ composite electrode as spherical particles that form a percolated network between the dense electrolyte to the current collector in a complex particle network (Bouvard and Lange, 1991). The distribution of the Ni and YSZ phase in the particle network is linked to the effective conductivities and the active TPB and expressed as functions of particle sizes, phase volume fractions and packing structure (Sanyal *et al.*, 2010). Metcalfe (2008), Abbaspour *et al.* (2010) and Kenney *et al.* (2009) have developed geometrical models which numerically reconstruct the porous composite electrode geometry and are used to evaluate the active TPB length in composite electrodes. The predictive capabilities of percolation and coordination-number theory as well as numerically reconstructed porous electrode geometry is greatly enhanced with the combination of a three-dimensional image reconstruction of a composite electrode that can be used to predict active TPB lengths and effective transport

properties of the electrode.

1.1.3 Shift towards nanostructured electrodes

The advancement in characterization of SOFC electrodes has led to research to further improve the electrochemical activity of the SOFC anode and to overcome the shortcomings of anode-supported SOFCs. One disadvantage of utilizing an anode support layer is susceptibility to structural changes due to the formation of nickel oxide during redox cycling. This ultimately leads to the cracking of the electrolyte, resulting in cell failure. A solution is to fabricate anodes by first preparing a porous YSZ network structure and subsequently infiltrating Ni. The porous YSZ network is fabricated by tape casting or slip casting 8mol % Y_2O_3 stabilized ZrO_2 powder with a pore former, usually 50 vol% graphite. The Ni is infiltrated onto the porous YSZ structure using molten $Ni(NO_3)_2 \cdot 6H_2O$ at 80^0C and after each infiltration, the molten Ni nitrate is decomposed to Ni oxide at 300^0C (Klemensø *et al.*, 2010). Multiple infiltrations is required to achieve sufficiently high electronic conductivity (Klemensø *et al.*, 2010; Jiang, 2006).

The porous YSZ structure provides the skeletal backbone to provide the mechanical support for the cell while the nanosized Ni particles form a semi-continuous film on the YSZ support framework, providing an electron conduction pathway that transport the electrons from the TPB to the current collector. The semi-continuous nature of the Ni film on the porous YSZ network has been reported by Busawon *et al.* (2008). A SEM image of the Ni film on the porous YSZ network is shown in Figure 1.2. It has been proposed that Ni infiltration could address the redox cycling problem experienced by the composite Ni anodes as Ni is no longer a part of the mechanical backbone (Sholklapper *et al.*, 2008). There is more flexibility for the Ni to contract and expand with changes in the chemical environment of the anode without generating mechanical strain or stress. In addition, the distinct interface between the support layer and the electrolyte is eliminated because the mechanical support and the electrolyte are of the same material and they are co-sintered at high temperatures,

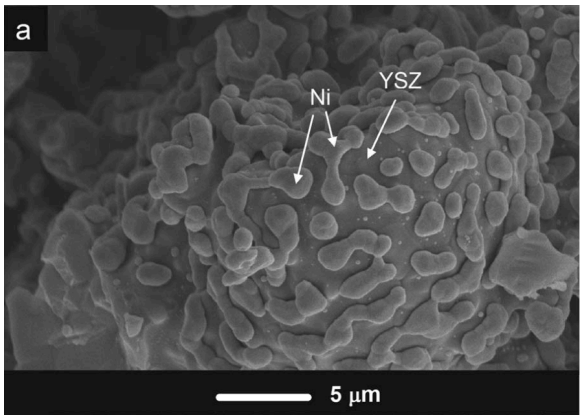

Figure 1.2: SEM image adopted from Busawon *et al.* (2008), showing the semi-continuous nature of the Ni film on the porous YSZ network

resulting in a well connected YSZ network which is mechanically robust (Torabi *et al.*, 2012). Another advantage of the infiltration method is the presence of nanosized Ni particles forming a semi-continuous film on the YSZ framework. Infiltrated nanosized particles have been linked to higher electrochemical performance in LSM infiltrated cathodes and metal-supported SOFCs with infiltrated electrodes (Sholklapper *et al.*, 2008; Tucker *et al.*, 2007). The nanosized particles are due to heat treatments at a much lower temperature when compared to the heat treatments experienced by composite electrodes as significant grain growth is observed when composite electrodes are sintered and reduced at 1400^0C (Jiang *et al.*, 2005).

It has been found that for an infiltrated anode system, a high performance can be achieved even at low Ni loading (Klemensø *et al.*, 2010). However, the optimal amount of Ni that must be impregnated to achieve acceptable electrochemical performance remains an open question. To answer this question, the amount of Ni in the porous structure would need to be related to its pertinent effective properties (effective conductivity and active TPB length). To get those effective properties, the unique Ni-infiltrated microstructure on the YSZ framework needs to be captured. Unfortunately, there are no models in the

literature that provide a relationship between Ni-content (Ni loading) and reaction sites for an infiltrated electrode system. Once the relationship between Ni loading and its pertinent effective properties is established, those properties are implemented into a porous model to determine the how Ni loading influences the electrochemical performance of a Ni-infiltrated porous anode.

1.1.4 Motivation and Objective

The significant differences between the microstructure of a conventional, composite Ni-YSZ SOFC anode and an Ni-infiltrated SOFC anode motivated the development of a numerical model for impregnated Ni-anodes that describe the semi-continuous morphology of Ni and its effect on electrochemical performance. Mathematical models that capture the structural impacts on the electrochemical performance of composite electrodes have been well established in literature (Sanyal *et al.*, 2010; Zhu and Kee, 2008; Abbaspour *et al.*, 2010; Kenney *et al.*, 2009). While the FIB-SEM experimental technique of reconstructing a 3D image of an electrode can be reapplied for a Ni-infiltrated SOFC anode system, the mathematical models that correlate microstructural parameters of the composite electrodes to electrochemical performance are not appropriate for Ni-infiltrated SOFC anode system.

The ultimate goal of this thesis is to simulate the electrochemical performance of a Ni-infiltrated SOFC anode so as to quantify the effect of key experimentally controlled parameters. To attain this goal, another objective of this thesis is to develop a model that describes the properties of Ni-infiltrated semi-continuous film. Figure 1.3 illustrates the hierarchy of models, including the relevant output of each model, that are developed in this thesis.

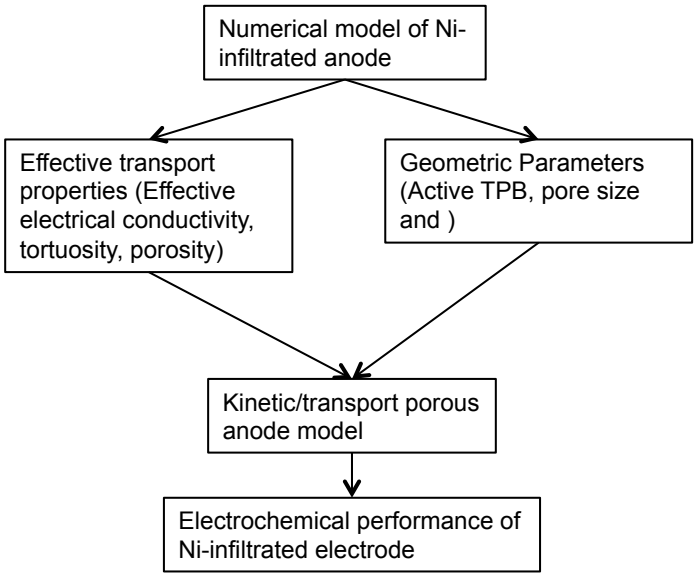

Figure 1.3: Hierarchy of models that have been developed in this thesis.

1.2 Thesis Structure

This thesis is organized in manuscript-style format and two manuscripts detailing the development of a numerical modeling framework of the Ni-infiltrated porous YSZ-supported solid oxide fuel cells are presented.

Chapter 2 focuses on the development of a novel semi-continuous film model based on percolation theory. This model is the *first* of its kind to relate the Ni semi-continuous film microstructure in Ni-infiltrated electrodes to pertinent effective properties of the SOFC anode.

Chapter 3 establishes a comprehensive multiphysics model that accounts for detailed electrochemistry, gas-phase porous media transport and charge transport in the electrodes and electrolyte for numerical simulation of electrochemical performance of the Ni-infiltrated porous YSZ-supported solid oxide fuel cells. Chapter 3 utilizes the results of the work presented in Chapter 2. Specifically, the effective properties (effective electronic conductivity and triple phase boundary lengths) estimated by the semi-continuous film model to correlate the effects of the Ni-loading to the electrochemical performance of the Ni-infiltrated anode from a cell-level perspective.

Chapter 2

Effective properties of semi-continuous film with application to solid oxide fuel cells

Chapter 2 presents the first manuscript of this thesis and focuses on developing a model that captures the semi-continuous nature of the Ni-film when it is infiltrated into a porous YSZ electrolyte network. The microstructural properties of the semi-continuous film is then related to the Ni loading and effective properties (effective electronic conductivity and triple phase boundary length) that are crucial to the function of the SOFC electrode. The manuscript is presented from a general thin films perspective and narrowed down specifically in estimating the effective properties of the Ni-infiltrated YSZ-supported SOFC. In addition, a conductivity degradation model framework that expanded on the semi-continuous film model provides quantification of the loss of reaction sites (TPB length) in a Ni-infiltrated anode expressed a function of degradation time.

2.1 Introduction

The development of thin film technology depends on being able to reliably predict the physical properties of the film which in turn requires a good understanding of how the film behaves when deposited on a substrate. Understanding the behaviour of thin films deposited on a substrate allows the optimization of the fabrication process as well as the operating conditions. The above approach has been used successfully for the manufacture of integrated circuit devices where thin films of metallic and insulating materials of precise dimensions are deposited on semiconductor surfaces (Grovenor *et al.*, 1984; Maissel and Glang, 1970).

The structure of metal films deposited on an inert substrates is dependent on the fabrication process. The deposition process for metal films can span from physical vapour deposition, such as pulsed laser deposition to chemical vapour deposition, for example, metal-organic chemical vapour deposition. The film growth for most metallic films deposited on inert substrates is characterized by the transformation of the film from a distribution of isolated particles to isolated clusters of particles and to a conglomerate of connected clusters that percolate from one end of the substrate to the other and finally a fully-continuous films as the film loading increases (Aziz, 2008). An illustration of the different stages of conductive film deposition on the substrates is shown in Figure 2.1.

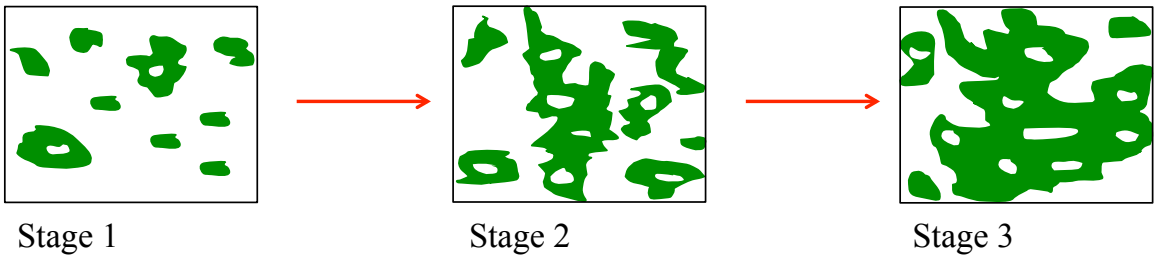

Figure 2.1: Schematic diagram depicting the growth of a conductive film (green) on an inert substrate (white) from a distribution of isolated particles to a conglomerate of connected clusters. Adapted from Aziz (2008).

This work uses a numerical simulation approach to provide insight into the effective properties of a semi-continuous metallic films deposited on an inert substrate. The effective properties of these films were correlated to film loading using percolation theory. Percolation theory describes how random clusters of particles form a connected network and the effects this has on the physical properties of the system. In addition, percolation theory is useful in identifying the size and shape of percolated clusters for use in applications where the connectivity of the clusters leads to active reaction sites (Stauffer and Aharony, 1994). As experimental identification of and differentiation between the percolated and isolated clusters is difficult, the use of a geometrical percolation model provides an alternative method to determine the connectivity of the clusters and the distribution of the inactive clusters.

Most of the work in literature that utilizes percolation theory to estimate effective conductivities of its electrically conductive film considers the film to be deposited onto a planar substrate (Yamamuro *et al.*, 1999; Wang *et al.*, 2005). In our work, we are interested in the deposition of electrically conductive film onto a porous substrate. The effective properties of metallic films that are deposited onto porous substrate will differ from when they are deposited onto planar substrates. Porous substrates, compared to dense and planar substrates, have pore spaces that the film will penetrate, directly influencing its effective properties. For instance, the effective conductivity of a film that is deposited onto a porous substrate will be a function of its conduction volume and its surface tortuosity on the porous substrate. The above mentioned effects are illustrated in Figure 2.2.

The presence of the pore space introduces volumetric effects such that the film's effective conductivity is dependent on the volume fraction of the deposited film. In addition, the film's effective conductivity is affected by the connectivity of the film's surface paths on the porous substrate. This connectivity is related to the surface tortuosity factor. The surface tortousity factor of the film accounts for the elongated electron travel path as a result of the film's three dimensional microstructure and is expressed as a function of porosity (Zalc *et al.*, 2003). In this work, we introduce strategies to allow the use of percolation theory

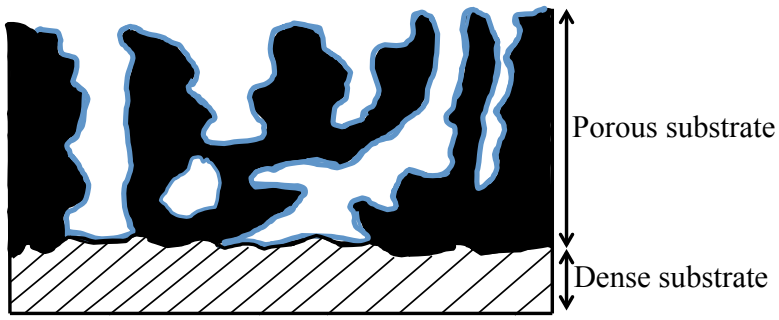

Figure 2.2: Schematic diagram illustrating the effect that film volume and surface tortuosity will have on properties such as effective conductivity of a porous inert structure with an infiltrated conductive film. The diagram is a cross-sectional slice of a porous substrate after the deposition of a metallic film. The porous substrate is depicted in black and the film in blue.

methods for films deposited on porous substrates.

2.1.1 Solid oxide fuel cell anodes

This work will focus on modeling solid oxide fuel cell anodes which are porous structures with two solid phases: an electro-catalyst and an electrolyte. The common material set for solid oxide fuel cell anodes is Nickel/Yttria-stabilized zirconia (Ni/YSZ) where the nickel functions as an electronic conductor that transports the electrons from reaction sites to the current collector. Yttria-stabilized zirconia functions as the ionic conductor that carries the oxygen ions from the electrolyte to the reaction sites. Conventionally, solid oxide fuel cell anodes consists of an intermingled network of percolated Ni and YSZ particles that extends from the dense electrolyte to the anode current collector (Singhal and Kendall, 2003). A percolated network of nickel provides the anode a connected pathway for electron transport as well as catalytic reaction sites for fuel oxidation. Fuel oxidation in SOFCs is represented by equation [2.1], with hydrogen gas as the fuel:

$$H_2 + O^{2-} \rightarrow H_2O + 2e^- \tag{2.1}$$

As fuel oxidation includes species from three different phases (gas, electronic and ionic), the reaction will only take place where all three phases co-exist, known as the triple phase boundary (TPB). A schematic diagram of a solid oxide fuel cell with a close-up of the porous electrode illustrating the TPB is shown in Figure 2.3.

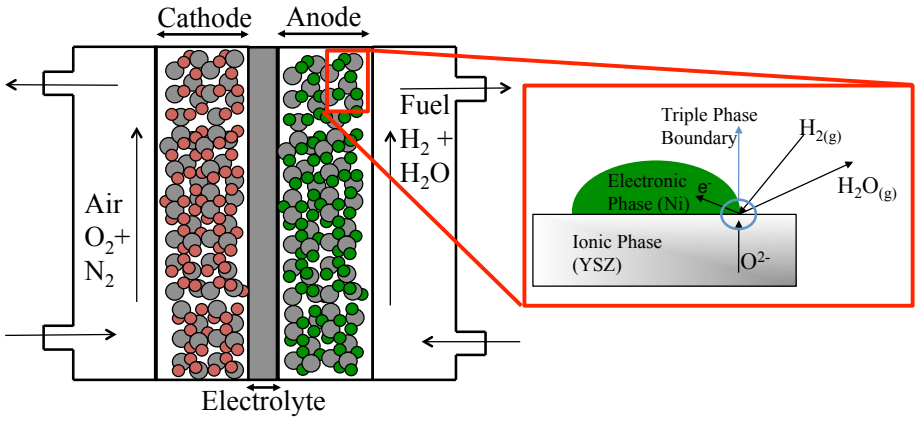

Figure 2.3: Schematic diagram illustrating solid oxide fuel cell with a close-up of the porous electrode depicting the triple phase boundary (TPB).

In recent years, significant effort has been focused on developing electrocatalyst infiltrated solid oxide fuel cell electrodes. These efforts have been motivated by the enhanced electrochemical performance of infiltrated electrodes (Sholklapper *et al.*, 2007) as well as their ability to avoid structural degradation due to redox cycling (Busawon *et al.*, 2008). An infiltrated Ni/YSZ anode is fabricated by first preparing the YSZ network structure to provide a mechanical support as well as a continuous transport network for oxygen ion transport. This structure, also called the YSZ support layer is porous, allowing transport of gaseous reactants and products. The Ni is then infiltrated into the porous YSZ and forms a semi-continuous film on the YSZ support framework (Busawon *et al.*, 2008).

In this work, we extend and generalize our earlier work (Hardjo *et al.*, 2011) to present a detailed model to evaluate key properties of electrically-conductive films on a porous insulting substrate and demonstrate its application to Ni-infiltrated solid oxide fuel cell electrodes.

2.2 Methodology

We propose a geometrical model for calculating the active perimeter and effective electrical conductivity of a electrically-conductive film on a porous insulating substrate based on percolation theory.

The electrically-conductive film is modeled as a two-dimensional (2D) film on a three-dimensional (3D) porous insulating substrate and the film is assumed to consist of overlapping circular disks that form a lattice with a specified coordination number. An illustration of the sintered film particles is shown in Figure 2.4.

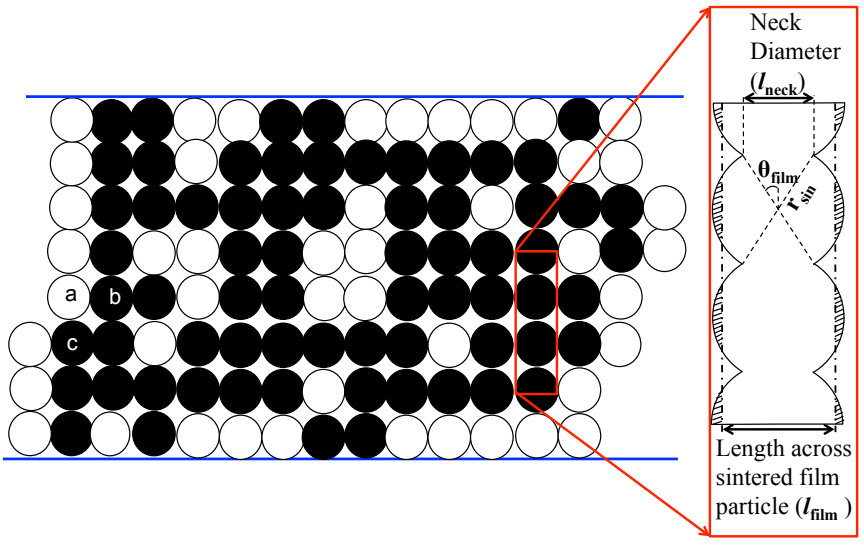

Figure 2.4: Schematic diagram showing the conductive film network. A close-up of the film particles overlapping each other is shown on the right hand side. The empty site (Particle a) represents a perimeter site that is adjacent to 2 occupied sites (Particles b and c).

In this work, we assume that the porous substrate framework consists of spherical insulating particles that have undergone sintering, resulting in overlapping spheres. The electrically conducting film is then deposited on the porous substrate and the growth of the 2D film on the porous substrate is modeled using percolation theory. When the substrate particles undergo sintering, it will result in the loss of spherical caps (Figure 2.5(a)) from the particles as the particles fuse with one another. The mass of the substrate is conserved during sintering and this results in the increase of the radius of the sintered substrate particles. The radius of the sintered substrate particle (see Figure 2.5(b)) is calculated using

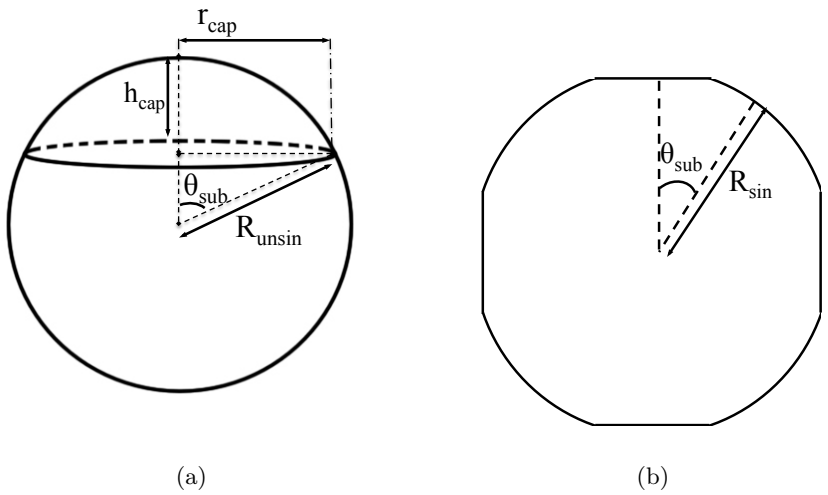

Figure 2.5: (a) 3D schematic diagram of a unsintered particle (b) 2D cross-section of a spherical particle describing the effects of sintering on the substrate particles. The notations on the diagrams are used in equation [2.2].

equation [2.2]:

$$\frac{4}{3}\pi R_{sint}^3 - \left[\pi h_{cap}\left(\frac{3(R_{cap})^2 + h_{cap}^2}{6}\right)\right] Z_{sub} = \frac{4}{3}\pi R_{unsint}^3 \tag{2.2}$$

In equation [2.2], the radius of the spherical cap $R_{cap} = R_{sint} sin(\theta_{sub})$ and the height of the spherical cap $h_{cap} = R_{sint} - R_{sint} cos(\theta_{sub})$. The available surface area of the substrate framework, A_{sub}, is evaluated by considering an unsintered substrate particle with a

coordination number Z_{sub} and an average particle radius of R_{unsint}.

$$A_{sub} = [4\pi R_{sint}^2) - 2\pi R_{sint} h_{cap} Z_{sub}] \cdot N \tag{2.3}$$

N represents the total number of substrate particles in a given volume and is given by equation [2.4]:

$$N = \frac{V_{sub}}{\frac{4}{3}\pi R_{sin}^3} \tag{2.4}$$

The conductive film particles will also undergo sintering and the above-mentioned calculation of the radius of a sintered substrate particle can be modified to reflect the 2D geometry of the conductive film particles. The film particles are assumed to be circular disks that are coordinated in a square lattice. The film's surface area, A_{film}, as a function of site occupation, p and the particle's packing factor, f_{pack} is captured by equation [2.5]:

$$A_{film} = p \cdot f_{pack} \cdot A_{sub} \tag{2.5}$$

In order to achieve a percolated system, the site occupation, p, has to be above the critical site occupation, p_c. p_c is a function of the chosen lattice and values for various lattices have been reported in Scher and Zallen (1970) and are summarized in Table 2.1:

Table 2.1: Critical percolation probability as a function of coordination number (Scher and Zallen, 1970)

Lattice	Coordination number (Z)	Packing factor (f_{pack})	Critical site occupation (p_c)
Triangular Lattice	6	0.9069	0.50
Square Lattice	4	0.7854	0.59

2.2.1 Estimation of perimeter of percolation network for a electrically-conductive film

When the film particles are deposited onto the porous substrate, they are randomly distributed across the porous network which results in either disconnected isolated particles

or the formation of clusters of film particles that are connected to each other and they will grow in size as more material is deposited. A percolated cluster is a cluster that connects all the way across the entire framework of the substrate (Bunde and Kantelhardt, 2005). Statistically, only isolated clusters exist below the percolation threshold and percolated clusters appear after the surface coverage of the film exceeds the percolation threshold.

The probability that an occupied site belongs to the percolated networks P_π is given by equation [2.6]. This allows us to differentiate the sites that belongs to percolated clusters from the sites that make up the isolated clusters.

$$P_\pi = k_\pi (p - p_c)^{\frac{5}{36}} \tag{2.6}$$

The proportionality constant k_π is calculated by concluding that once all the film particles have covered the substrate framework in a square lattice configuration, the fraction of film particles that belong to the percolated cluster will be unity. Rearranging equation [2.6] and solving for k_π, we obtain $k_\pi = 1.13$ for a square lattice. Once the fraction of sites that belong to the percolated network is determined, the active perimeter of the conductive film can be determined using a cluster perimeter analysis outlined by Stauffer and Aharony (Stauffer and Aharony, 1994). They defined the perimeter of a cluster τ as the number of empty sites neighbouring occupied sites in a cluster and it is represented by equation [2.7]. The perimeter as defined includes internal holes in the cluster as well as the external empty sites that enclose the cluster.

$$\tau = n_\pi \left(\frac{1-p}{p} \right) + 4(n_\pi)^{0.5} \tag{2.7}$$

The number of film particles that make up the percolating networks n_π can be evaluated by dividing the surface area of the percolated conductive film by the surface area of one disk-like film particle. To compute the physical length of the perimeter, we need to first relate τ to the total number of occupied sites on the perimeter. We assume that the perimeter sites are associated with, on average, two occupied sites (Refer to Figure 2.4). With the above assumption, the active perimeter length of the percolated film (ℓ_{peri}) can be expressed as

equation [2.8]:

$$\ell_{peri} = 2[(\pi - 2\theta_{film})r_{sin}]\tau \tag{2.8}$$

where θ_{film} is the contact angle of the film particles. For a SOFC anode, the active perimeter length is equivalent to the TPB length as described in Figure 2.3.

2.2.2 Estimation of effective electrical conductivity

The electrical resistance of a semi-continuous film deposited on a porous substrate is higher than the resistance of a solid conductive sample of identical dimensions. This increased resistance of porous materials due to geometric effects is usually quantified by defining an effective conductivity for the material σ_{eff}.

The ratio of the effective conductivity to the bulk conductivity σ_0 can be expressed as a summation of three factors as represented by equation [2.9]:

$$\sigma_{eff} = \sum_{i=1}^{3} \sigma_{eff}^{i} \tag{2.9}$$

The first effect takes the connectivity of a semi-continuous conducting film on an insulating substrate into account. We use equation [2.10] proposed in Stauffer and Aharony (1994) to calculate the effective conductivity as a function of site occupation p.

$$\sigma_{eff}^{1} = k_{cond}(p - p_c)^{1.3} \tag{2.10}$$

The second effect σ_{eff}^{2} is due to the assumed geometrical structure of the film and is caused by current constriction in the necks between particles (see Figure 2.4). The film consists of sintered conductive particles and the necks between the sintered film particles lead to constrictions in the flow of current. The constriction effect is investigated by comparing the resistances of the sintered film and a continuous film. The resistance of the continuous film is given by equation [2.11].

$$R_{cont} = \frac{1}{\sigma_0}\left(\frac{L}{A_x}\right) \tag{2.11}$$

L is the length of the continuous film element, A_x is the cross-sectional area of the continuous

film. The resistance of the sintered particle is evaluated by numerically solving for the current given a specified applied voltage across constricted (with a neck) sintered particle. The ratio of the resistance of the sintered particle to the resistance of the continuous film is a function of contact angle between the interacting particles (see Figure 2.6). The effect of the constrictions decreases as the contact angle between the interacting particles increases as seen in Figure 2.6. The third effect σ_{eff}^3 comes from the three dimensional structure of the

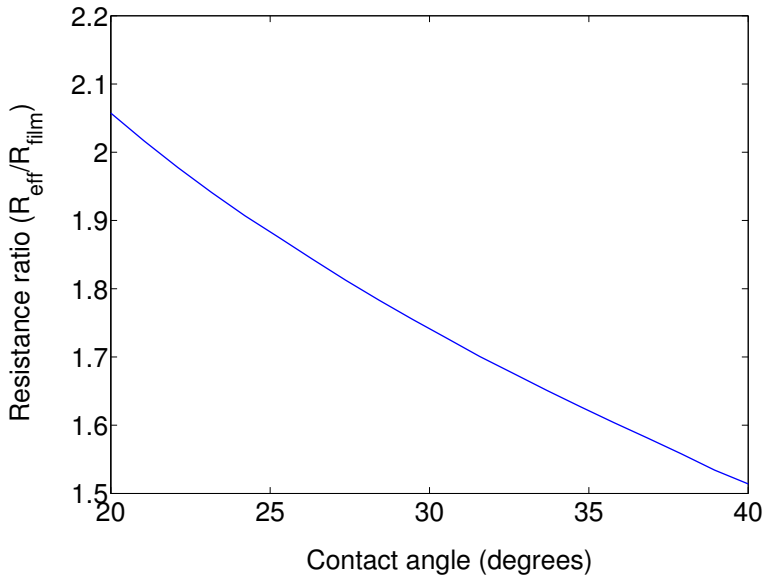

Figure 2.6: Resistance ratio between the sintered film particle and the film resistance as a function of contact angle.

porous substrate on which the film is deposited and is a function of the bulk volume fraction of the conducting phase V_{film} and surface tortousity of the film τ_s. We use equation [2.12] to express the ratio of the resistance due to this volumetric effect to the bulk conductivity of the film σ_0.

$$\sigma_{eff}^3 = \frac{V_{film}}{\tau_s}\sigma_0 \tag{2.12}$$

τ_s can be determined by adopting the work of Zalc *et al.* (2003) where they have correlated

the surface tortuosity of the film to the void fraction of the solid. The final expression for the effective conductivity is given by equation [2.13]:

$$\sigma_{eff} = \underbrace{\frac{V_{film}}{\tau_s} \cdot \frac{R_{eff}}{R_{film}} \cdot \frac{1}{(1-p_c)^{1.3}} \cdot \sigma_0}_{k_{cond}} \cdot (p - p_c)^{1.3} \tag{2.13}$$

2.2.3 Relating site occupation to volume of film

In the preceding subsections, we have developed relationships for effective properties as a function of site occupation, p. However, as most experimental studies on conducting films report effective conductivity as a function of the volume of the conducting material, we need to relate p to the volume of the conductive film, V_{film}. The volume of the conductive phase is given by the product of the effective surface coverage of the conductive film and the thickness of the film. We propose two scenarios in which V_{film} can be related to p: When the film is deposited onto the porous substrate, the growth of the film can occur in two ways:

1. The film can grow in both surface area, A_{film} and thickness, t_{film}
2. The film only grows in surface area and have a constant thickness

Film thickness as a function of coverage

Šmilauer (1991) reported that the change of thickness of the film above the percolation threshold, $t - t_c$, is proportional to the change of site occupation above percolation threshold, $p - p_c$. This is represented by Equation [2.14].

$$t_{film} - t_c = k_t(p - p_c) \tag{2.14}$$

Equation (2.14) requires knowledge of the thickness proportionality constant k_t. k_t is expressed as a function of critical film thickness t_c and a reference site occupation p_{ref} with

its corresponding thickness t_{ref} using equation [2.15].

$$k_t = \frac{t_{ref} - t_c}{p_{ref} - p_c} \tag{2.15}$$

To evaluate k_t, we need the critical film volume fraction V^c_{film} to determine t_c and p_{ref} with its corresponding thickness t_{ref}. V^c_{film} is defined as the film volume fraction for which there is a presence of percolated film clusters that allows for the conduction of electrons and it can be determined experimentally. t_c is represented by Equation [2.16].

$$t_c = \frac{V^c_{film}}{A^c_{film}} \tag{2.16}$$

The critical film surface coverage is evaluated using equation [2.5] where $p = p_c$. To obtain t_{ref} as a function of p_{ref}, we use an experimentally available data point (σ_{eff}, V_{film}) as follows: The value of p_{ref} for the chosen data point (σ_{eff}, V_{film}) is obtained rearranging equation [2.13] and substituting the value for σ_{eff}. The corresponding t_{ref} is calculated by Equation [2.17] where A_{ref} is again given by Equation 2.5.

$$t_{ref} = \frac{V_{film}}{A_{ref}} \tag{2.17}$$

Constant thickness film

If we assume that the film thickness does not change with coverage, then t_{film} is given by Equation [2.18]

$$t = t_c = \frac{V_c}{A_c} \tag{2.18}$$

In this case the site occupation and the area of the film increases linearly as more conductive material is deposited.

2.3 Application to Ni-infiltrated solid oxide fuel cell anodes

In this section, we use our model to predict the effective properties for Ni-impregnated solid oxide fuel cell anodes. Both scenarios for film growth mechanism mentioned in the previous section are implemented and compared. We adopt the experimental results (Table

2.2) reported by Klemensø *et al.* (2010) for our model. We chose to use an average particle size of 100nm for the Ni particles as it was reported (Busawon *et al.*, 2008) that there is a wide distribution of particle sizes from 50nm to 200nm.

The effective properties obtained from our model are then compared to the effective properties for the conventional (composite) Ni-YSZ solid oxide fuel cell electrodes which are modeled using percolation theory as outlined by Zhu and Kee (2008). The parameters for the conventional composite electrode model are given in Table 2.3. The model results

Table 2.2: Model parameters used to calculate effective properties for an infiltrated Ni anode

Parameter	Description	Numerical Value
ϕ_{open}	Open porosity of porous substrate	0.43
V_{YSZ}	YSZ Volume fraction	0.57
R_{YSZ}	Radius of YSZ particles	$0.5 \times 10^{-6} m$
r_{Ni}	Radius of Ni particles	$50 \times 10^{-9} m$
V_{Ni}^{ref}	Reference Ni volume fraction	0.155
σ_{ref}	Reference effective conductivity	716 $\frac{S}{cm}$
V_{film}^{c}	Critical Ni volume fraction	0.075

Table 2.3: Model parameters used to calculate effective properties for a composite Ni-YSZ anode

Parameter	Description	Numerical Value
ϕ_{open}	Open porosity of porous substrate	0.4
V_{YSZ}	YSZ Volume fraction	0.6
R_{YSZ}	Radius of YSZ particles	$0.5 \times 10^{-6} m$
r_{Ni}	Radius of Ni particles	$0.5 \times 10^{-6} m$
V_{Ni}^{c}	Critical Ni volume fraction	0.21

for effective conductivity are for an operating temperature of 800C. The TPB length and effective conductivity for a Ni infiltrated anode and a conventional Ni-YSZ anode obtained using the parameters in Tables 2.2 and 2.3 are presented in Figures 2.7(a) and 2.7(b).

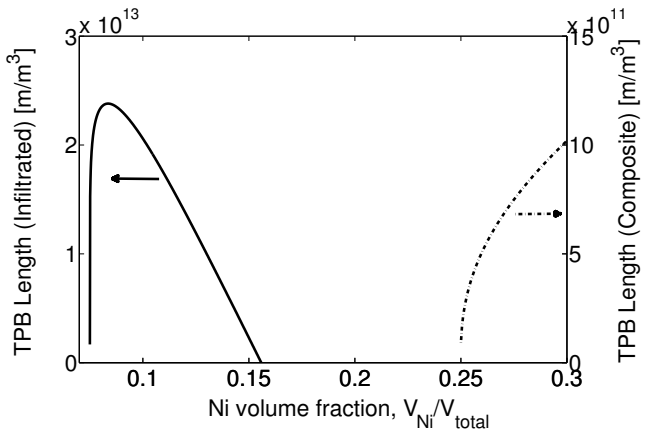

(a)

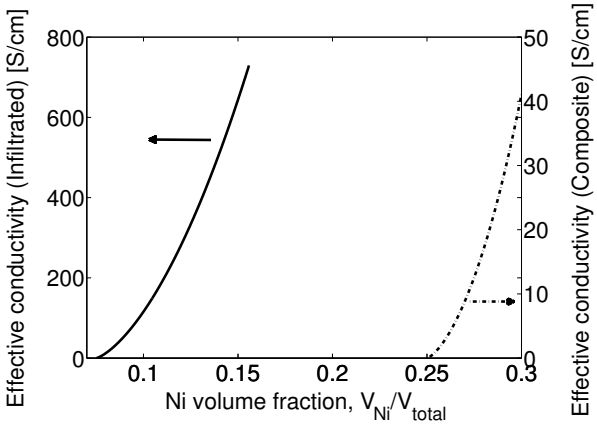

(b)

Figure 2.7: (a) Active TPB length $[m/m^3]$ vs. Ni volume fraction for an infiltrated Ni anode and a conventional Ni-based SOFC anode. (b)Effective conductivity [S/cm] vs. Ni volume fraction for an infiltrated Ni anode and a conventional Ni-based SOFC anode. Model parameters are given in Table [2.2] and [2.3]

From Figure 2.7(a), the active TPB length for an infiltrated electrode goes through a maximum as opposed to the monotonically increasing active TPB length for composite electrodes. The composite electrodes will also show a decrease in active TPB length with increasing Ni loading. The maximum in active TPB length can be explained as follows. While the surface coverage of Ni increases with increased Ni volume fraction, after a certain point the perimeter decreases such that the TPB length at full coverage would be zero. The decrease in perimeter length corresponds with internal holes in the percolating cluster getting smaller with increasing coverage and connectivity of the percolating Ni film. A key result seen clearly in Figure 2.7(a) is that infiltrated electrodes are able to achieve much higher TPB lengths than composite electrodes. This implies that infiltrated electrodes should be capable of generating higher currents than composite electrodes. This is borne out by experimental studies which report very good performance for infiltrated electrodes (Sholklapper *et al.*, 2007).

Figure 2.7(b) indicates that infiltrated electrodes are able to achieve sufficient electrical

conductivities when compared to composite electrodes at a much lower Ni loading. These results agree with the findings in experimental literature (Busawon *et al.*, 2008; Singh and Krishnan, 2008)

The two film growth scenarios as outlined in the methodology section affect the on effective conductivity and TPB lengths as shown in Figures 2.8(a) and 2.8(b). From Figures 2.8(a) and 2.8(b), it is evident that the film growth mechanism significantly influences the predicted effective properties.

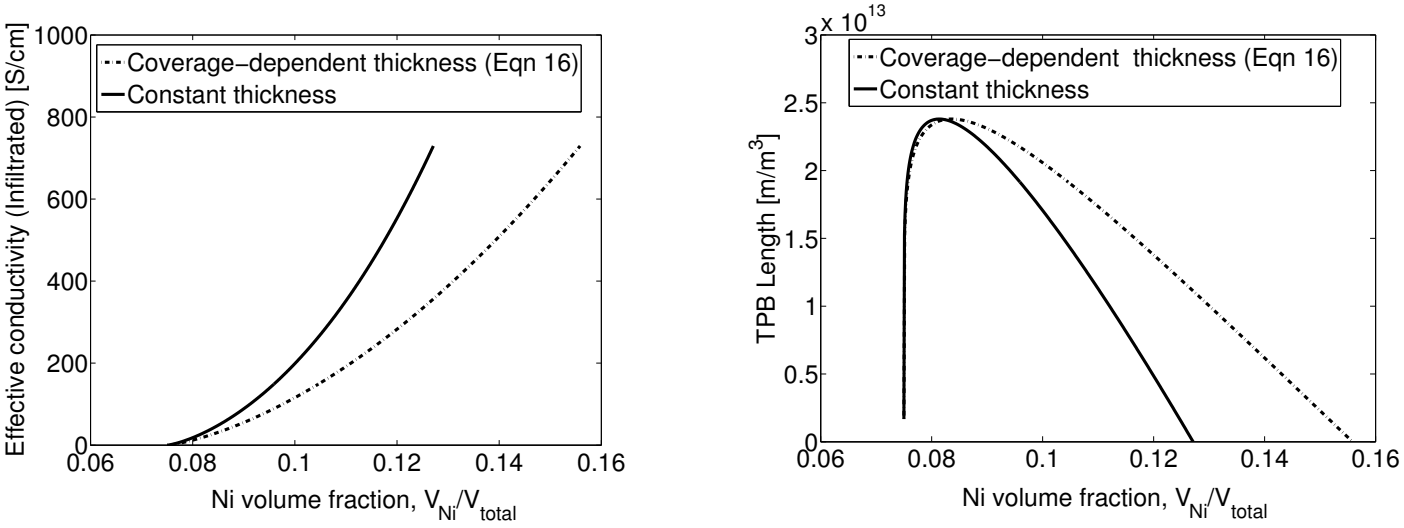

(a) (b)

Figure 2.8: (a) Effect of film growth mechanism on effective conductivity [S/cm] vs. Ni volume fraction of an infiltrated Ni-based anode. (b) Effect of film growth mechanism on TPB lengths vs. Ni volume fraction of an infiltrated Ni-based anode. Model parameters are outlined in Table [2.2] and [2.3].

2.3.1 Sensitivity Analysis

A sensitivity analysis is carried out to determine how effective properties of the Ni-impregnated SOFC electrode are affected by changes in key experimentally obtained parameters. The first analysis is the investigation of how sensitive the effective properties are to changes in

the critical Ni volume fraction (V^c_{film}). V^c_{film} depends on the morphology of the substrate as well as the film and is found to vary significantly. We vary V^c_{film} from 0.06 to 0.08 and its effect on effective conductivity (σ_{eff}), TPB lengths (ℓ_{TPB}) and film thickness (t_{film}) are shown in Figure 2.9(a) - 2.9(c).

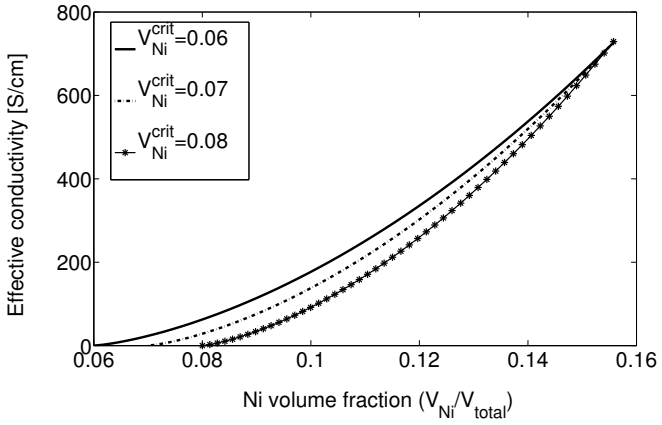

(a)

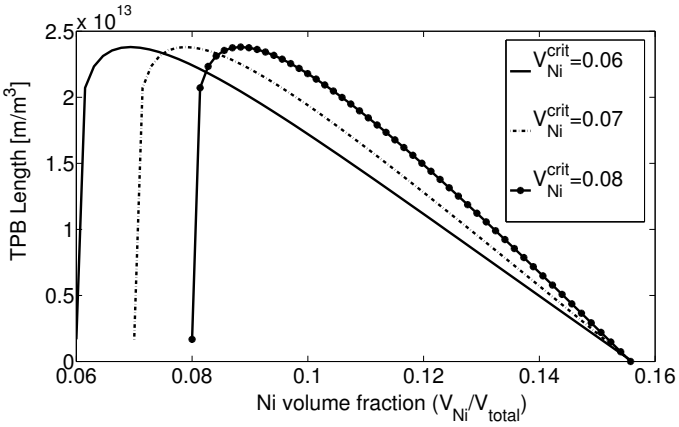

(b)

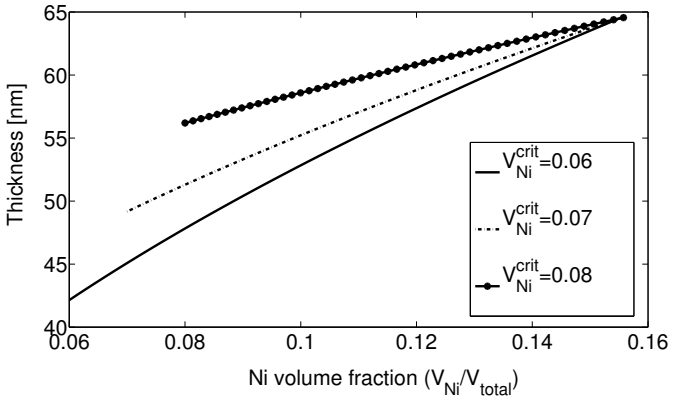

(c)

Figure 2.9: (a) Effective conductivity vs. Ni volume fraction as a function of V^c_{film} (b)TPB length vs. Ni volume fraction as a function of V^c_{film} (c) Thickness of Ni film vs. Ni volume fraction as a function of V^c_{film}. The simulation conditions are outlined in Table [2.2].

Figure 2.9(a) shows that as V^c_{film} increases, the effective conductivity curves are shifted so that they start at the corresponding V^c_{film}. It should also be noted that by using a reference conductivity measurement (σ_{ref}) to determine k_{thick}, the effective conductivity curves are forced to go through the reference conductivity measurement data point. The experimental data point (V_{Ni}=0.16, σ_{eff}=716.7 $\frac{S}{cm}$) was extracted from the work of Klemensø *et al.* (2010). This causes the conductivity curve to change its slope as V^c_{film} changes to accommodate the value of σ_{ref} that is used to determine k_{thick}. Figure 2.9(b) and Figure 2.9(c) show similar trends as the effective conductivity curves with a change in V^c_{film}.

The second analysis examines the sensitivity of effective properties to the particle size of the Ni particles r_{Ni}. The Ni radius was varied from 50nm to 100nm and its effect on ℓ_{TPB} Figure 2.10 shows that as expected, ℓ_{TPB} increases as r_{Ni} decreases. We verified that changing the Ni radius does not impact σ_{eff} and t_{film}. σ_{eff} and t_{film} depend on the effective surface area coverage of the Ni on YSZ and a change in r_{Ni} will not have an impact on these properties as long as p or A_{Ni} does not change. The increase in r_{Ni} causes a decrease in the number of nickel particles that cover the porous YSZ, this results in loss of perimeter of the percolated networks.

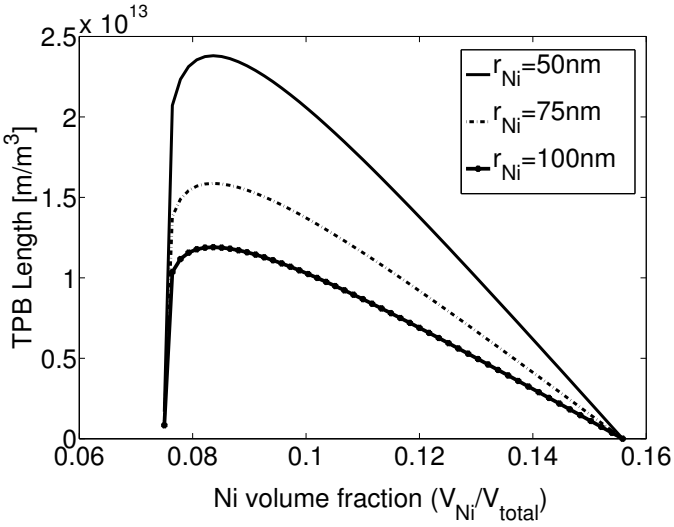

Figure 2.10: TPB sensitivity to r_{Ni}. The simulation conditions are outlined in Table [2.2] and r_{Ni} was varied from 50nm to 100nm.

The third analysis is the investigation of how sensitive the effective properties are to the particle size of YSZ particles R_{YSZ}. R_{YSZ} was varied from 0.5 μm to 1.5 μm. Figure 2.11(a) and Figure 2.11(b) show that t_{film} is directly proportional to R_{YSZ} while ℓ_{TPB} is inversely proportional to R_{YSZ}.

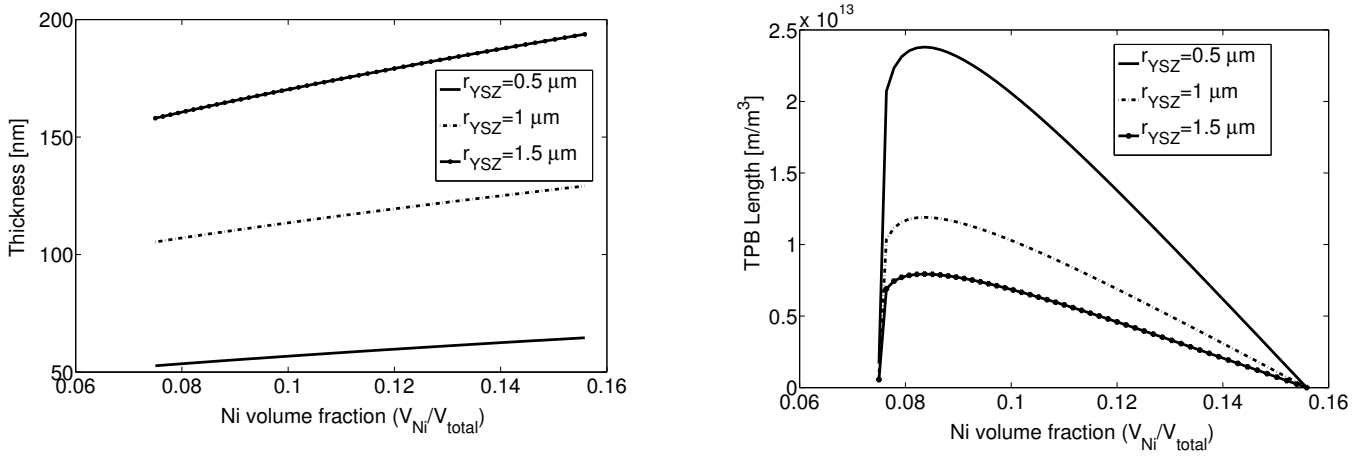

(a) (b)

Figure 2.11: (a)Thickness sensitivity to R_{YSZ}. (b)TPB sensitivity to R_{YSZ}. The simulation conditions are outlined in Table [2.2] and R_{YSZ} was varied from 50nm to 100nm.

The above analysis reveals that the effective properties of Ni infiltrated anodes can be influenced to a large degree by the experimentally determined input parameters and it further shows that the fabrication process of the YSZ framework as well as the Ni infiltration process have a significant impact on the effective properties.

From observing the trends in the effective properties (σ_{eff}, ℓ_{TPB} and t_{film}) as a function of the key experimentally determined parameters (V^c_{film}, r_{Ni} and r_{YSZ}), it can be concluded that higher values of ℓ_{TPB} can be obtained by reducing the particle sizes for both Ni and YSZ. A YSZ framework that consists of small particles will result in a high surface area, which will allow more Ni particles to be deposited onto the YSZ framework. Similarly, a Ni film that consists of small Ni particles will result in a higher TPB length.

2.4 Degradation of Ni film on porous YSZ electrode

When the interfacial energies between the deposited electrically-conducting film and the insulating substrate are high, the elevated operating temperature will initiate an agglomeration phenomena. Agglomeration of the metallic films is a thermally-activated mass transport process which decreases the surface area of the film in order to reduce the surface energies between the film and the substrate (Boragno *et al.*, 2009). It causes a semi-continuous film to break up into isolated islands and thereby losing connectivity of the film across the substrate. Agglomeration of metallic films that are deposited on inert substrates has been linked to performance degradations of conductive, metallic films deposited on an inert substrate as a result of disruptions in the connectivity of a once-continuous film (Gadkari *et al.*, 2005).

With a focus on SOFC anodes, degradation of electrochemical performance during SOFC operation for a composite anode has been linked to Ni particle coarsening due to the poor wettability between the Ni and YSZ phase (Tsoga *et al.*, 1996; Utz *et al.*, 2011). Similarly for a Ni-infiltrated SOFC, the semi-continuous Ni film that is formed on the porous YSZ framework will experience Ni coarsening and agglomeration of the Ni film will occur. Using the semi-continuous film model framework, we propose a degradation model that captures the agglomeration effect of the Ni film on the porous YSZ framework. The motivation for the development of a degradation model is to quantify the film's degradation to its percolated perimeter. The percolated perimeter of the film is a function of site occupation and the number of film particles that make up the percolating network. Therefore, with a change in site occupation as a result of agglomeration of the Ni film, the percolated perimeter will be affected accordingly. In the specific case of an SOFC anode, the change in the percolated perimeter results in a change in the TPB length, directly affecting the number of reaction sites available in the electrode. Quantifying the change in TPB length as a function of degradation time is important in understanding the extent of performance degradation in

an Ni-infiltrated SOFC anode during long-term operation.

When Ni film agglomeration occurs, the Ni surface coverage decreases and the thickness of the film increases, in order to conserve the total Ni volume of the film. The degradation model utilizes conductivity degradation data and correlates the decrease in conductivity as a function of time back to the site occupation, $p_{degrade}$. $p_{degrade}$ has been defined to distinguish the different scenarios in which the variable, p, is being used. In this case, $p_{degrade}$ is specific to the degradation of site occupation with respect to time. The film's effective conductivity equation, equation [2.13], as derived in the previous section is expressed as a function of the film's microstructural properties. It can be rearranged to solve for the site occupation, $p_{degrade}$ and expressed as a function of conductivity degradation data. The conductivity degradation data as a function of time is directly used to track the devolution of the semi-continuous film. The rearranged form of the film's effective conductivity equation is given in equation [2.19]:

$$\left[\frac{\sigma_{eff}}{\frac{V_{film}}{\tau_s}\cdot\frac{R_{eff}}{R_{film}}\cdot\frac{1}{(1-p_c)^{1.3}}\cdot\sigma_0}\right]^{1/1.3} + p_c = p_{degrade} \tag{2.19}$$

Once the degradation of site occupation as a function of time has been determined, it can be related back to the surface area of the film via equation [2.20], thus determining how the surface area is changing as a function of time during the Ni agglomeration process.

$$A_{film} = p_{degrade}\cdot f_{pack}\cdot A_{sub} \tag{2.20}$$

Since the Ni volume will be conserved during the degradation of the film, the change in thickness of the film with respect to degradation time can be determined by taking the ratio of the Ni volume fraction and the surface area of the film as a function of degradation time. Using the model parameters defined in Table [2.2] to calculate the effective properties for an infiltrated Ni anode and conductivity degradation data as reported by Klemensø *et al.* (2010), we express the site occupation degradation, TPB length degradation and change in thickness as a function of degradation time. The conductivity degradation data extracted

from Klemensø *et al.* (2010) is specific to a Ni volume fraction of 0.09.

From Figure 2.12, it can be observed that the TPB degradation is directly correlated to the conductivity degradation. The conductivity of the Ni film degrades over time due to loss of connectivity of the semi-continuous film which results in isolated Ni islands. The increase in isolated Ni islands results in a decrease in active TPB lengths.

The conductivity degradation model that builds upon the Ni semi-continuous film model achieves some degree of success in capturing the agglomeration effect of the Ni film on the porous YSZ framework and allowing us to quantify the TPB length degradation as a function of degradation time.

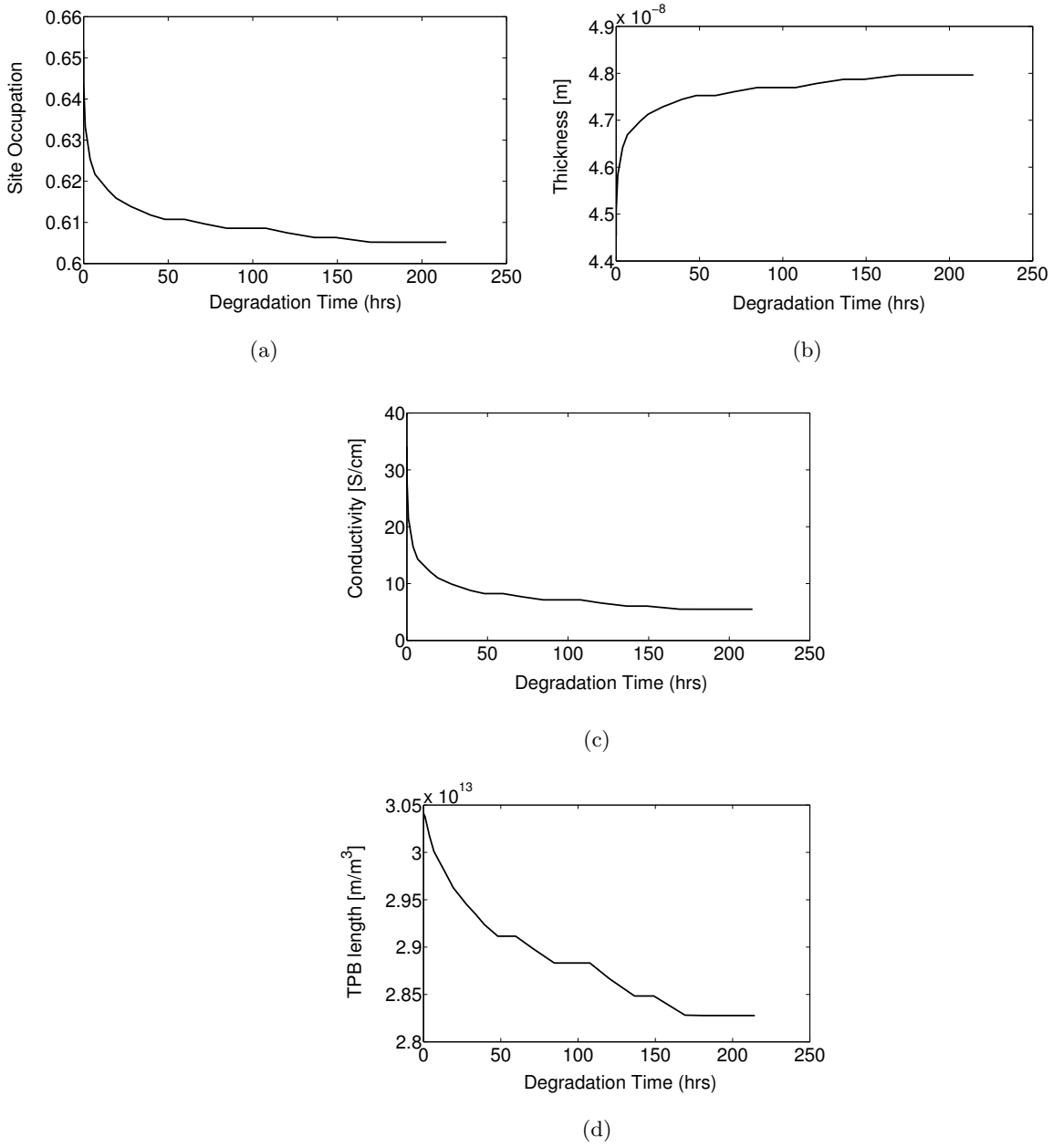

Figure 2.12: (a) The site occupation of the Ni film on the porous YSZ framework as a function of degradation time (b) The thickness of the Ni film on the porous YSZ framework as a function of degradation time (c) Conductivity degradation data from Klemensø *et al.* (2010) as a function of degradation time. (d) TPB degradation as a function of degradation time. The simulation conditions are outlined in Table [2.2].

2.5 Conclusion

We develop a model based on percolation theory that predicts the effective properties of conducting semi-continuous films deposited on an insulating substrate. This model is applied to Ni-infiltrated SOFC anodes to estimate the effective electronic conductivity and TPB length as a function of various physical parameters. Comparison of effective electronic conductivity and TPB lengths for a Ni-infiltrated anode with those for a composite Ni-YSZ anode suggests that an infiltrated Ni anode with adequate electrical conductivity and sufficiently high TPB length can be manufactured even at a very low Ni loading. Our model uses experimental data and agrees with the trends reported in the literature but thorough validation must await further targeted experiments. We expect that the validation process will help refine the several assumptions inherent in the model. Our results demonstrate the film growth mechanism has a significant impact on the effective properties of the film. The properties of a conductive film deposited onto a porous substrate are highly dependent on the manufacturing conditions of the porous substrate as well as the deposition process. In addition, a conductivity degradation model framework that expanded on the semi-continuous film model allows us to quantify the loss of reaction sites in a Ni-infiltrated anode as a function of degradation time.

Chapter 3

Electrochemical model of Ni-infiltrated porous anode

The manuscript presented in this chapter provides a comprehensive description of the development of an electrochemical performance model that considers the coupled gas-phase transport phenomena, charge transport in the electrodes and electrolytes and the electrochemical kinetics. The fundamental electrochemistry occurring at the the SOFC anodes is also discussed in detail. The development of a 2D multiphysics porous electrode model uses the novel semi-continuous film model that was developed in Chapter 2 to estimate the effective properties of the Ni-infiltrated electrodes that will be used as input parameters in the porous electrode model.

3.1 Introduction

Anode-supported solid oxide fuel cells (SOFCs) has been identified as a promising cell design for operation at lower temperatures because of its low ohmic resistance contribution from the thin dense electrolyte and a thick anode layer that provides mechanical support for the cell without compromising transport of the gas phase species (Jiang, 2006). However, the

anode support layer is susceptible to structural changes due to the formation of Nickel oxide and reduction to Nickel during redox cycling. This ultimately leads to the cracking of the electrolyte, resulting in cell failure.

One solution to address this problem is to fabricate anodes by first preparing a porous YSZ network structure and subsequently infiltrating Ni. The porous YSZ structure provides the skeletal backbone to provide the mechanical support for the cell while the nanosized Ni particles form a semi-continuous film on the YSZ support framework, providing an electron conduction pathway that transport the electrons from the TPB to the current collector (Busawon *et al.*, 2008). The semi-continuous nature of the Ni film on the porous YSZ network has been reported by Busawon et al. and an SEM image of the Ni film on the porous YSZ network is shown in Figure 3.1.

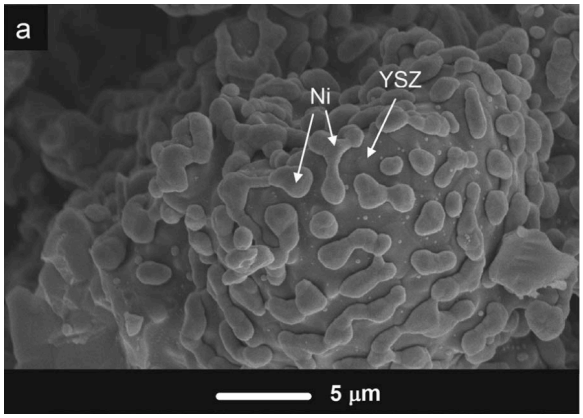

Figure 3.1: SEM image adopted from Busawon *et al.* (2008). It depicts the semi-continuous nature of the Ni film on the porous YSZ network

Since the Ni is not a part of the mechanical backbone, there is more flexibility for the Ni to contract and expand upon changes in the chemical environment on the anode side. In addition, the distinct interface between the support layer and the electrolyte is eliminated because the mechanical support and the electrolyte are of the same material and they are co-sintered at high temperatures, resulting in a well connected YSZ network which

is mechanically robust (Gorte and Vohs, 2009; Torabi *et al.*, 2012). Another advantage in the infiltration method is the presence of nanosized Ni particles forming a semi-continuous film on the YSZ framework (Busawon *et al.*, 2008). Infiltrated nanosized particles have been linked to higher electrochemical performance in LSM infiltrated cathodes and metal-supported SOFCs with infiltrated electrodes (Sholklapper *et al.*, 2008; Tucker *et al.*, 2007). The nanosized particles are achieved due to heat treatments at a much lower temperature when compared to the heat treatments experienced by composite electrodes as significant grain growth is observed when composite electrodes are sintered and reduced at 1400^0C (Jiang *et al.*, 2005).

It has also been reported that a much lower Ni loading is required for an infiltrated electrode to achieve a comparable electrical conductivity to composite electrodes (Klemensø *et al.*, 2010). However, the optimal amount of Ni that must be impregnated remains an open question. Too much Ni impregnation may cause suppression of TPB whereas too little may result in a largely unconnected Ni network and therefore low active reaction sites. We take a numerical modelling approach to determine optimal amount of Ni that must be impregnated to achieve optimal electrochemical performance. Mathematical models that capture the structural impacts on the electrochemical performance of composite electrodes have been well established in literature. On the other hand, an appropriate numerical model for impregnated Ni-anodes that describe the semi-continuous morphology of Ni and its effect on electrochemical performance has not yet been reported.

We have previously developed a semi-continuous film on a porous substrate geometrical model that allows us to estimate the effective conductivities and TPB lengths of the infiltrated film. In this paper, we examine the electrochemical performance of an infiltrated anode with comparison to a conventional composite anode. We will then use our semi-continuous film to extract the effective properties of the Ni-infiltrated film and use it as inputs onto a fully coupled multiphysics model. The focus of this work is on the anode polarization behaviour of the SOFC in order to directly compare the effects of Ni loading

and microstructural differences between the infiltrated anode and the composite anode. In addition, the electrochemical performance results that includes the cathodic effects and determine its role in influencing the cell's current output is also presented.

3.2 Model Domain

The first geometry considered is a Ni-infiltrated porous YSZ anode-only cell depicted in Figure 3.2(a). To focus on the anode microstructural effects on electrochemical performance, an ideal cathode boundary condition is implemented at the cathode/electrolyte interface and an ideal dense YSZ electrolyte is used. The ideal cathode boundary condition assumes that all losses associated with the cathode are negligible. An ideal dense YSZ electrolyte is applied by assuming a high ionic conductivity such that ohmic losses at the dense electrolyte is negligible.

The half-cell Ni-infiltrated porous YSZ network geometry is further modified to represent a Ni-infiltrated "bi-layer" YSZ supported SOFC anode. It consists of a Ni-infiltrated support layer and a composite Ni-YSZ functional layer that is representative of the cells that are fabricated at University of Calgary (See section 3.7.2). The second geometry is a 2D full cell model as shown in Figure 3.2(b) which considers either an Ni-infiltrated YSZ support layer or a composite Ni-YSZ complemented with a composite LSM-YSZ cathode.

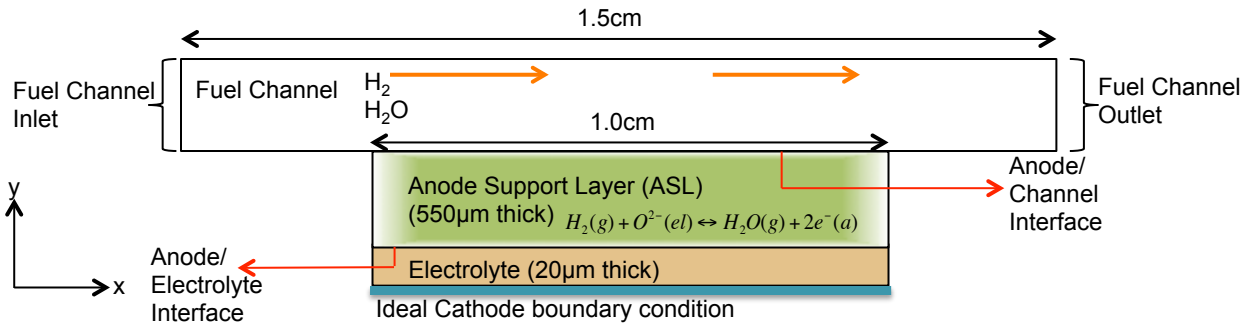

(a) Schematic diagram of a half-cell Ni-infiltrated porous YSZ electrode

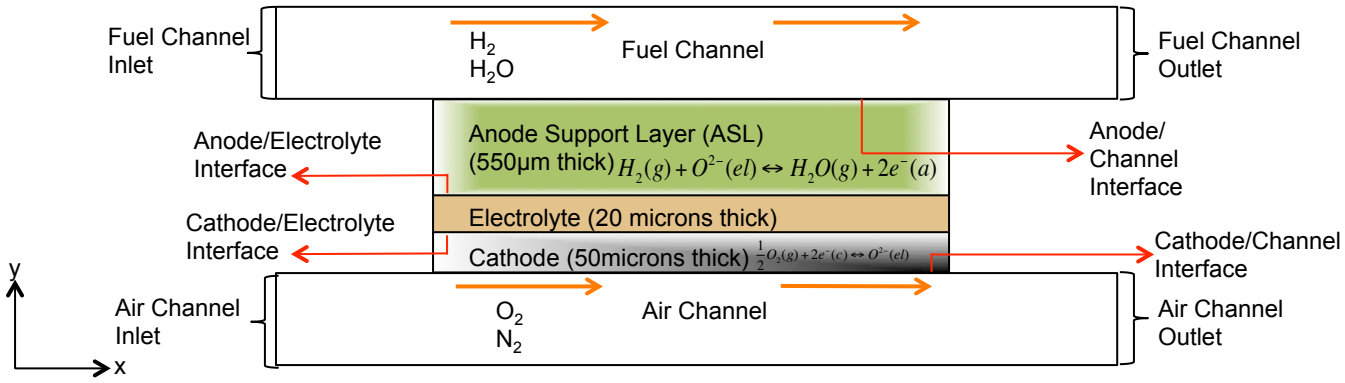

(b) Schematic diagram of a full-cell Ni-infiltrated porous YSZ electrode complemented with a composite LSM-YSZ cathode.

Figure 3.2: Schematic diagrams of cell geometry considered

3.3 Modeling Approach

3.3.1 Electrochemistry

We take a more fundamental and elementary approach in modeling the electrochemistry of an SOFC. We adopt the work of Zhu *et al.* (2005) where they have described the charge-transfer reactions in terms of mass-action kinetics. In their work, they utilized a hydrogen oxidation mechanism developed by de Boer (1998) that comprises of five elementary reactions (Equations [3.1] to [3.5]) occuring at the Ni-YSZ TPB region. They have also considered a single two-step charge transfer reactions for the electrochemical reduction of oxygen at the LSM-YSZ TPB region (Equations [3.13] to [3.14]). Using the elementary

charge-transfer reactions at the anode and at the cathode, they developed a Butler-Volmer like expression relating the anodic and cathodic current density to the local electric phase potentials, surface coverages and gas phase species. Here, we present the main equations required to solve the modified Butler-Volmer equations as developed by Zhu *et al.* (2005). A more detailed discussion on SOFC electrochemistry is presented in Appendix A.

Anode electrochemistry

$$\begin{gathered} H_2(g) + 2s_{ads,ed}(a) \underset{k_{-1}}{\overset{k_1}{\rightleftharpoons}} 2H_{ads,ed} \\ K_1 = \frac{\theta_H^2}{\theta_{Ni}^2 p_{H2}} \end{gathered} \tag{3.1}$$

For the adsorption reaction, $s_{ads,ed}(a)$ represents an empty Nickel site, $H_{ads,ed}$ represents an adsorbed hydrogen molecule on the Nickel surface. θ_H is the fractional surface coverage of the adsorbed hydrogen molecule on the Nickel surface and θ_{Ni} is the fractional free Nickel surface sites.

$$\begin{gathered} H_{ads,ed} + O^{2-}_{ads,el} \underset{k_{-2}}{\overset{k_2}{\rightleftharpoons}} s_{ads,ed}(a) + OH^-_{ads,el} + e^-_{ed} \\ K_2 = \frac{\theta_{Ni}\theta_{OH}}{\theta_H \theta_O} exp(-\frac{F\Delta\phi_a}{RT}) \end{gathered} \tag{3.2}$$

$O^{2-}_{ads,el}$ represents an oxygen ion absorbed on YSZ surface, $OH^-_{ads,el}$ represents an hydroxide ion absorbed on YSZ surface. e^-_{ed} represents an electron within the Nickel. θ_{OH} is the fractional surface coverage of the adsorbed hydroxide ion on the YSZ surface. θ_O is the fractional surface coverage of the oxide ion on the YSZ surface.

$$\begin{gathered} H_{ads,ed} + OH^-_{ads,el} \underset{k_{-3}}{\overset{k_3}{\rightleftharpoons}} s_{ads,ed}(a) + H_2O_{ads,el} + e^-_{ed} \\ k_3 = k_3^0 \theta_H \theta_{OH} exp(\frac{\beta_{3f} F\Delta\phi_a}{RT}) \end{gathered} \tag{3.3}$$

$$k_{-3} = k_{-3}^0 \theta_{H_2O} \theta_{Ni} exp(-\frac{\beta_{3r} F\Delta\phi_a}{RT})$$

$H_2O_{ads,el}$ represents an absorbed water molecule on YSZ surface. θ_{H2O} is the fractional surface coverage of the water molecule on the YSZ surface.

$$\begin{gathered} H_2O_{ads,el} \underset{k_{-4}}{\overset{k_4}{\rightleftharpoons}} H_2O(g) + s_{ads,el} \\ K_4 = \frac{\theta_{YSZ} p_{H2O}}{\theta_{H2O}} \end{gathered} \tag{3.4}$$

$s_{ads,el}$ represents an empty YSZ site. θ_{YSZ} represents the fractional free YSZ surface sites.

$$\begin{gathered} O_o^x(ads,el) + s_{ads,el} \underset{k_{-5}}{\overset{k_5}{\rightleftharpoons}} O_{ads,el}^{2-} + V_o^{\cdot\cdot}(ads,el) \\ K_5 = \frac{\theta_{YSZ}}{\theta_O} \end{gathered} \tag{3.5}$$

$O_o^x(ads,el)$ represents a lattice oxygen on YSZ, $V_o^{\cdot\cdot}(ads,el)$ represents an oxygen vacancy on YSZ. θ_O is the fractional surface coverage of lattice oxygen on YSZ. The global half-cell anode reaction is expressed in equation [3.8]. Assuming that reaction [3.3] is rate-limiting, it follows that the rest of the reactions are proceeding at a fast rate and are at psuedo-equilibrium. Hence, the reactions [3.1 - 3.2] and reactions [3.4 - 3.5] are described using equilibrium constants. For electrochemically-active reactions, the equilibrium is dependent on the the electronic potential difference of the electron-conducting phase and the ionic potential of the oxygen-ion conducting phase. The modified Butler-Volmer equation is defined in Equation [3.6].

$$i_v = i_{0,H2}\left[exp\left(\frac{\alpha_a F \eta_{act}}{RT}\right) - exp\left(\frac{-\alpha_c F \eta_{act}}{RT}\right)\right] \tag{3.6}$$

where i_v is the distributed volumetric current density, $\alpha_{a,c}$ is the charge transfer coefficient and η_{act} is the local activation overpotential and is defined as $\eta_{act} = \Delta\phi - \Delta\phi_{eq}$. $\Delta\phi$ is defined as the difference between the electric phase potential of the electrode, ϕ_{ed} and the electric potential of the electrolyte, ϕ_{el} (Bessler *et al.*, 2007). $\Delta\phi_{eq}$ is the local equilibrium phase potential and is defined using the Nernst equation (Equation [3.7]).

$$\Delta\phi_{eq}^{an} = \mu_{H2O}^0 - \mu_{H2}^0 - \mu_{O^{2-}}^0 - \frac{RT}{2F} ln \frac{a(H_2)}{a(H_2O)} \tag{3.7}$$

which considers the global half-cell anode reaction (Equation [3.8]).

$$H_2(g) + O_{ads,el}^{2-} \rightleftharpoons H_2O(g) + V_o^{\cdot\cdot}(ads,el) + 2e_{ed}^- \tag{3.8}$$

$i_{0,H2}$ is the exchange current density for hydrogen oxidation and is defined in Equation [3.9]

$$i_{0,H2} = i^*_{H2} \left(\frac{p_{H2}}{p^*_{H2}}\right)^{\frac{\alpha_a - 1}{2}} \left(\frac{p_{H2O}}{p_{atm}}\right)^{\frac{\alpha_a}{2}} \left[1 + \left(\frac{p_{H2}}{p^*_{H2}}\right)^{1/2}\right]^{-1} \tag{3.9}$$

i^*_{H2} is the exchange current factor for the anodic current density. It is a function of the TPB length, λ_{TPB}, rate and equilibrium constants from the hydrogen oxidation elementary reactions, determined at a reference temperature (Equation [3.10]).

$$i^*_{ref,H2} = 2\lambda_{TPB} F k_{-3} \left(\frac{k_3}{k_{-3}} K_2\right)^{0.25} \left(\frac{K_5}{K_4}\right)^{0.75} \tag{3.10}$$

The i^*_{H2} dependance on temperature is given in Equation [3.11].

$$i^*_{H2} = i^*_{ref,H2} exp\left[\frac{-E_{a,H2}}{R}\left(\frac{1}{T} - \frac{1}{T_{ref}}\right)\right] \tag{3.11}$$

$i^*_{ref,H2}$ is fitted to measured polarization data for a composite electrode button cell at a reference temperature. Alternatively, $i^*_{ref,H2}$ can be normalized with respect to the TPB length, λ_{TPB}, such that it will be a dimensionless quantity and a function of only the rate and equilibrium constants of the elementary charge transfer reactions. In our work, we use the $i^*_{ref,H2}$ of $4.8 \times 10^3 \frac{A}{cm^3}$ reported by Zhu and Kee (2008). The parameter, p^*_{H2}, is defined in Equation [3.12].

$$p^*_{H2} = \frac{A_{des}\Gamma\sqrt{2\pi M_{H2}}}{\gamma_0\sqrt{RT}} exp\left(\frac{-E_{des}}{RT}\right) \tag{3.12}$$

where A_{des} is the pre-exponential factor for the H_2 desorption reaction, E_{des} is the activation energy for the desorption reaction and Γ is the surface site density of Nickel, γ_0 is the sticking coefficient of hydrogen gas absorption onto Nickel. The derivation of p^*_{H2} is given in Appendix A.

Cathode electrochemistry

In this work, we will model the cathode electrochemistry by considering the oxygen reduction to occur in two elementary reactions expressed in Equations [3.13] and [3.14]. We adopt the work of Zhu *et al.* (2005) and use their Butler-Volmer like equation to solve the current density at the cathode as a function of local electric phase potentials, surface coverages and

gas phase species at the cathode.

$$O_{2(g)} + 2s_{ads,ed}(c) \underset{k_{-6}}{\overset{k_6}{\rightleftharpoons}} 2O_{ads,ed}(c)$$
$$K_6 = \frac{\theta_c^2 p_{O2}}{\theta_O^2} \tag{3.13}$$

For the adsorption reaction, $s_{ads,ed}(c)$ represents an empty LSM site. $O_{ads,ed}(c)$ represents an absorbed oxygen molecule on the cathode surface site. $\theta_O(c)$ is the fractional surface coverage of the adsorbed oxygen molecule on the LSM surface and θ_c is the fractional free LSM surface sites.

$$O_{ad(c)} + V_o^{\cdot\cdot}(el) + 2e^-(c) \underset{k_{-7}}{\overset{k_7}{\rightleftharpoons}} O_o^x(el) + (c)$$

$$k_7 = k_7^0 \theta_c exp(\frac{\beta_{7f} F \Delta\phi_c}{RT}) \tag{3.14}$$

$$k_{-7} = k_{-7}^0 \theta_O exp(-\frac{\beta_{7r} F \Delta\phi_c}{RT})$$

We then use equation [3.6] to describe the current density as a function of local phase overpotentials, surface coverages and partial pressures of the gaseous species. We express the exchange current density for the cathode, $i_{0,O2}$ using equation [3.15].

$$i_{0,O2} = i_{O2}^* \left[\frac{p_{O2}}{p_{O2}^{\alpha_c/2}}\right] \left[1 + \left(\frac{p_{O2}}{p_{O2}^*}\right)^{1/2}\right]^{-1} \tag{3.15}$$

An Arrhenius form of p_{O2}^* has been reported by Zhu *et al.* (2005). It is derived in the same manner as p_{H2}^* by considering the equilibrium reaction O_2 adsorption on LSM and expressing the oxygen surface coverage, $\theta_O(c)$ as a function of K_6 and the partial pressure of O_2.

$$p_{O2}^* = A_{O2} exp\left(-\frac{E_{O2}}{RT}\right) \tag{3.16}$$

A_{O2} is defined as the pre-exponential factor for the O_2 desorption reaction on LSM and E_{O2} is defined as the activation energy for the oxygen desorption reaction on LSM. i_{O2}^* is the exchange current factor for the cathodic current density. It is a function of the TPB length, ℓ_{TPB}, rate and equilibrium constants from the oxygen reduction elementary

reactions, determined at a reference temperature (Equation 3.17).

$$i^*_{ref,O2} = 2\ell_{TPB} F k_7 K_7^{-0.5} \tag{3.17}$$

The i^*_{O2} dependance on temperature is given in Equation 3.18.

$$i^*_{O2} = i^*_{ref,O2} exp\left[\frac{-E_{a,O2}}{R}\left(\frac{1}{T} - \frac{1}{T_{ref}}\right)\right] \tag{3.18}$$

$i^*_{ref,O2}$ is fitted to measured polarization data for a composite electrode button cell at a reference temperature. Alternatively, $i^*_{ref,O2}$ can be normalized with respect to the TPB length, ℓ_{TPB}, such that it will be a dimensionless quantity and a function of only the rate and equilibrium constants of the elementary charge transfer reactions. In our work, we use the $i^*_{ref,O2}$ of $5.6 \times 10^4 \frac{A}{cm^3}$ reported by Zhu and Kee (2008).

3.3.2 Coupled Multiphysics Transport Processes

We have developed a fully-coupled multiphysics model to capture the microstructural impact of an infiltrated anode on its performance. The model considers the following physics:

1. Multicomponent species transport without reaction in the gas channels.
2. Multicomponent species transport with reaction in porous media(electrode).
3. Momentum transport in the gas channels.
4. Momentum transport in the porous media.
5. Charge transport (electrons and oxygen ions) in the porous electrodes.

Multicomponent species transport without reaction in the gas channels

The multicomponent species transport in the gas channel is solved using the Maxwell-Stefan formulation (Equation [3.19]).

$$\nabla \cdot \left[\rho \omega_i u \ - \rho_i \sum_{\substack{j=1 \\ i \neq j}}^{n} \tilde{D}_{ij} \left[\nabla x_j + (x_j - \omega_j) \frac{\nabla p_g}{p_g} \right] \right] = 0 \tag{3.19}$$

where ρ is the density of the gas mixture, ρ_i is the density of species i, ω_i is the mass fraction of species i, x_j is the mole fraction of species j, p_g is the total gas pressure, $\tilde{D}_{ij}$ is defined as multicomponent Fick diffusivity and it is related to the binary diffusion coefficients via Equation [3.20].

$$\begin{aligned} \tilde{D}_{ii} &= -\frac{\omega_j^2}{x_i x_j} D_{ij} \\ \tilde{D}_{jj} &= -\frac{\omega_i^2}{x_i x_j} D_{ij} \\ \tilde{D}_{ij} = \tilde{D}_{ji} &= -\frac{\omega_i \omega_j}{x_i x_j} D_{ij} \end{aligned} \tag{3.20}$$

The binary diffusion coefficients, D_{ij} are determined using the empirical correlation determined by Krishna and Wesselingh (1997).

$$D_{ij} = \frac{3.16 \times 10^{-8} T^{1.75}}{p \left(v_i^{\frac{1}{3}} + v_j^{\frac{1}{3}} \right)^2} \left[\frac{1}{M_i} + \frac{1}{M_j} \right]^{0.5} \tag{3.21}$$

v_i and v_j are molar diffusion volumes. M_i and M_j are the molecular weights of species i and j respectively.

A full derivation of the Maxwell-Stefan formulation from the convection-diffusion equation is discussed in the Appendix B.

Multicomponent species transport with reaction in porous media

The same set of equations as derived for the multicomponent species transport in the gas channels applies with the addition of the reaction term as gaseous species will be reacting

in the porous electrode when the cell is polarized. The final implicit form of the Maxwell-Stefan formulation used for multicomponent species transport in porous media is expressed in Equation [3.22].

$$\nabla \cdot \left[\rho \omega_i u \; - \rho_i \sum_{\substack{j=1 \\ i \neq j}}^{n} \tilde{D}_{ij} \left[\nabla x_j + (x_j - \omega_j) \frac{\nabla p_g}{p_g} \right] \right] = R_{a,c} \tag{3.22}$$

where $R_{a,c}$ is the reaction term with R_a representing the anode reaction term and R_c representing the cathode reaction term respectively. $R_{a,c}$ is expressed in Equation [3.23]:

$$R_a = \frac{\lambda^a_{TPB} i_v M_{H2}}{2F}$$
$$R_c = -\frac{\lambda^c_{TPB} i_v M_{O2}}{4F} \tag{3.23}$$

where F is Faraday's constant, i_v is the volumetric current density, λ^a_{TPB} is the TPB density associated with the anode and λ^c_{TPB} is the TPB density associated with the cathode and M_{H2} is the molecular weight of hydrogen and M_{O2} is the molecular weight of oxygen. In addition, two geometrical effects, porosity/tortuosity of the porous media and Knudsen diffusion, must also be considered when describing the multicomponent species transport in porous media.

Porosity and tortuosity of porous media

The effect of porosity, ϕ_g and tortuosity, τ_g of the porous media will be captured by using the effective binary diffusion coefficients for the gas-phase species. This is represented by Equation [3.24].

$$D^{eff}_{ij} = \frac{\phi_g}{\tau_g} D_{ij} \tag{3.24}$$

Knudsen diffusion

Knudsen diffusion occurs in porous media when the mean free path length in the gas is larger than the pore sizes of the porous medium. This increases the frequency at which the gas collides with the walls, increasing the effects of the wall surface interactions on the

flow characteristics (Atkins and De Paula, 2006). The Knudsen diffusion coefficient,D_i^K, for porous media is expressed in Equation [3.25].

$$D_i^K = \frac{2}{3}\frac{\phi_g}{\tau_g} r_{pore}\sqrt{\frac{8RT}{\pi M_i}} \tag{3.25}$$

where r_{pore} is the radius of the pore. To incorporate Knudsen diffusion in the multicomponent mass transport of porous media, we implement an averaged bosanquet binary diffusion coefficients (Equation [3.26]) that retains the cyclic symmetry of the Stefan-Maxwell diffusion coefficient and ensuring species mass conservation (Todd, 2003).

$$D_{ij}^{eff} = D_{ji}^{eff} = 0.5\frac{\phi_g}{\tau_g}\left(\frac{1}{1/D_i^K + 1/D_{ij}} + \frac{1}{1/D_j^K + 1/D_{ij}}\right) \tag{3.26}$$

A more detailed discussion on Knudsen diffusion is presented in the Appendix C.

Momentum transport in the gas channels

Navier-Stokes equations with composition-dependent viscosity is used to model the flow in the channels (Equation [3.27]) and is coupled to the continuity equation [3.28])

$$-\nabla\cdot\left[\mu_g\left(\nabla\mathbf{v} + (\nabla\mathbf{v})^T\right) - \frac{2}{3}\mu_g\left(\nabla\cdot\mathbf{v}\right)\mathbf{I}\right] + \rho\left(\mathbf{v}\cdot\nabla\mathbf{v}\right) + \nabla p_g = 0 \tag{3.27}$$

$$\nabla\cdot(\rho\mathbf{v}) = 0 \tag{3.28}$$

$\mathbf{v}$ is the velocity vector for the gas mixture, p_g is the gas pressure, $\mathbf{I}$ is the identity matrix and μ_g is the viscosity of gases. At low pressures, the viscosity of a gas can be calculated through the Chapman-Enskog relationship (Equation [3.29])

$$\mu_g = 26.69\times10^{-8}\frac{\sqrt{1000M_iT}}{\sigma_i^2\Omega_i^{2,2}(T^*)} \tag{3.29}$$

σ_i is the collision diameter for gaseous species, M_i is the molecular weight for species i and $\Omega_i^{2,2}(T^*)$ is the collision integral expressed as a function of reduced temperature. The tabulated values for $\sigma_i(nm)$ and $\Omega_i^{2,2}(T^*)$ can be found in the Appendix A of Brodkey and Hershey (1988). For a binary mixture at the anode and at the cathode, we use Equation

3.30 to determine an averaged viscosity for the mixture.

$$\mu_{mix} = 0.5 \left[\sum_{i=1} x_i \mu_i + \frac{1}{\sum_{i=1} \frac{x_i}{\mu_i}} \right] \tag{3.30}$$

Momentum transport in the porous media

The Navier-Stokes equation is modified to include Darcy's terms to account for the momentum transport in porous media (Equation [3.31]) and is coupled to the continuity equation [3.32]).

$$\left(\frac{\mu_g}{\kappa} + R_{a,c} \right) \mathbf{v} = \nabla \cdot \left[-p_g \mathbf{I} + \frac{\mu_g}{\epsilon} \left(\nabla \mathbf{v} + (\nabla \mathbf{v})^T \right) - \frac{2}{3} \mu_g \left(\nabla \cdot \mathbf{v} \right) \mathbf{I} \right] \tag{3.31}$$

$$\nabla \cdot (\rho v) = R_{a,c} \tag{3.32}$$

κ is the permeability of the gas and is expressed by the Carman-Kozeny relation for an aggregated bed of spheress in Equation [3.33]

$$\kappa = \frac{d_{pore}^2}{180} \frac{\epsilon^2}{(1-\epsilon)^2} \tag{3.33}$$

where d_{pore} is the mean diameter of the pore and is estimated using Equation [3.34].

$$d_{pore} = \frac{2\phi_g d_{particle}}{3(1-\phi_g)} \tag{3.34}$$

where $d_{particle}$ is the mean particle diameter $R_{a,c}$ is the reaction term associated with the anode, R_a or the reaction term associated with the cathode, R_c:

$$R_a = \frac{\lambda_{TPB}^a i_v \left(M_{H_2O} - M_{H_2} \right)}{2F} \tag{3.35}$$

$$R_c = -\frac{\lambda_{TPB}^c i_v (M_{O2})}{4F} \tag{3.36}$$

where λ_{TPB}^a is the TPB density associated with the anode and λ_{TPB}^c is the TPB density associated with the cathode.

Electronic and ionic charge transport

The electric and ionic potential fields are directly correlated to the electrochemical reaction rates at the anode and at the cathode and we describe the electric and ionic charge transport through the porous electrodes using the charge transport equations as defined in Equation [3.37].

$$\begin{aligned} \nabla \cdot (-\sigma_{ed(i)}^{eff} \nabla \phi_{ed(i)}) &= i_v \\ \nabla \cdot (-\sigma_{el}^{eff} \nabla \phi_{el(i)}) &= i_v \end{aligned} \tag{3.37}$$

$\sigma_{ed(i)}^{eff}$ is the effective electronic conductivity for electronic phase. $\sigma_{el(i)}^{eff}$ is the effective ionic conductivity for the ionic phase. $\phi_{ed(i)}$ is the electric phase potential for the electrode and $\phi_{el}(i)$ is the ionic phase potential for the electrolyte. i_v is the distributed volumetric current density as a function of TPB length and is expressed by Equation [3.6]. The intermingling of different material phases necessitates that the pertinent intrinsic transport properties be modified to account for the material phase distribution and interconnectivity as well as the tortuous path followed by the transported quantity. The intrinsic properties must therefore be modified to account for geometrical effects of the porous media. The effective properties of the semi-continuous Ni film on porous YSZ as a function of Ni loading using a geometrical model developed in our previous work discussed in Chapter 2. The effective properties of composite Ni-YSZ will be determined by using a widely-adopted percolation and coordination-number theory (Zhu and Kee, 2008). The percolation and coordination-number theory used to calculate the effective properties of composite SOFC electrodes are discussed in the Appendix D.

3.4 Governing equations and boundary conditions

Multicomponent species transport in gas channels

$$\nabla \cdot \left[\rho \omega_i u \; - \rho_i \sum_{\substack{j=1 \\ i \neq j}}^{n} \tilde{D}_{ij} \left[\nabla x_j + (x_j - \omega_j) \frac{\nabla p_g}{p_g} \right] \right] = 0 \tag{3.38}$$

Boundary conditions

1. Mass fraction of H_2 and O_2 is specified at the fuel channel inlet and air channel inlet respectively.

$$\omega_{H2}|_{\partial\Omega_{fuel,inlet}} = \omega_{H2,in} \tag{3.39}$$

$$\omega_{O2}|_{\partial\Omega_{air,inlet}} = \omega_{O2,in} \tag{3.40}$$

2. No flux condition is imposed at the walls of the channel

$$\mathbf{n} \cdot \mathbf{J_i}|_{\partial\Omega_{wall}} = 0 \tag{3.41}$$

   where $\mathbf{J_i}$ represents the total flux.

3. Continuity of fluxes is imposed at the channel/electrode interface.

$$\mathbf{J_i}|_{\partial\Omega_{channel/electrode}} = \mathbf{J_i}|_{\partial\Omega_{electrode/channel}} \tag{3.42}$$

4. Convective flux boundary condition was imposed at the fuel and air channel outlet.

$$\mathbf{n} \cdot \mathbf{J_i}|_{\partial\Omega_{fuel,outlet}} = \mathbf{n} \cdot \omega_i \rho \mathbf{u} \tag{3.43}$$

$$\mathbf{n} \cdot \mathbf{J_i}|_{\partial\Omega_{air,outlet}} = \mathbf{n} \cdot \omega_i \rho \mathbf{u} \tag{3.44}$$

Multicomponent species transport in porous media

$$\nabla \cdot \left[\rho \omega_i u \; - \rho_i \sum_{\substack{j=1 \\ i \neq j}}^{n} \tilde{D}_{ij} \left[\nabla x_j + (x_j - \omega_j) \frac{\nabla p_g}{p_g} \right] \right] = R_{a,c} \tag{3.45}$$

Boundary conditions

1. No flux condition is imposed at the walls of the porous media

$$\mathbf{n} \cdot \mathbf{J_i}|_{\partial\Omega_{wall}} = 0 \tag{3.46}$$

2. Continuity of fluxes is imposed at the channel/electrode interface.

$$\mathbf{J_i}|_{\partial\Omega_{channel/electrode}} = \mathbf{J_i}|_{\partial\Omega_{electrode/channel}} \tag{3.47}$$

Momentum transport in gas channels

$$-\nabla \cdot \left[\mu\left(\nabla\mathbf{v} + (\nabla\mathbf{v})^T\right) - \frac{2}{3}\mu\left(\nabla \cdot \mathbf{v}\right)\mathbf{I}\right] + \rho\left(\mathbf{v} \cdot \nabla\mathbf{v}\right) + \nabla p_g = 0 \tag{3.48}$$

$$\nabla \cdot (\rho\mathbf{v}) = 0 \tag{3.49}$$

Boundary conditions

1. Laminar, fully developed flow at the fuel and air inlets

2. No slip boundary conditions at the walls of the channel/porous electrode

$$\mathbf{v}|_{\partial\Omega_{wall}} = 0 \tag{3.50}$$

3. Continuity boundary conditions are enforced at the channel/porous electrode interface.

$$p_{channel}|_{\partial\Omega_{channel/electrode}} = p_{electrode}|_{\partial\Omega_{channel/electrode}} \tag{3.51}$$

$$\mathbf{v}_{channel}|_{\partial\Omega_{channel/electrode}} = \mathbf{v}_{electrode}|_{\partial\Omega_{channel/electrode}} \tag{3.52}$$

4. An atmospheric pressure, P_{atm}, boundary condition, normal to the outlets of the fuel and air channels are specified.

$$p_{channel}|_{\partial\Omega_{outlet}} = P_{atm} \tag{3.53}$$

Momentum transport in porous media

$$\left(\frac{\mu}{\kappa} + R_{a,c}\right)\mathbf{v} = \nabla \cdot \left[-p_g\mathbf{I} + \frac{\mu}{\epsilon}\left(\nabla\mathbf{v} + (\nabla\mathbf{v})^T\right) - \frac{2}{3}\mu\left(\nabla \cdot \mathbf{v}\right)\mathbf{I}\right] \tag{3.54}$$

$$\nabla \cdot (\rho v) = R_{a,c} \tag{3.55}$$

Boundary conditions

1. No slip boundary conditions at the walls of the channel/porous electrode

$$\mathbf{v}|_{\partial\Omega_{wall}} = 0 \tag{3.56}$$

2. Continuity boundary conditions are enforced at the channel/porous electrode interface.

$$p_{channel}|_{\partial\Omega_{channel/electrode}} = p_{electrode}|_{\partial\Omega_{channel/electrode}} \tag{3.57}$$

$$\mathbf{v}_{channel}|_{\partial\Omega_{channel/electrode}} = \mathbf{v}_{electrode}|_{\partial\Omega_{channel/electrode}} \tag{3.58}$$

Electron and ion transport in porous electrode

$$\begin{aligned} \nabla \cdot (-\sigma_{ed(i)}^{eff} \nabla \phi_{ed(i)}) &= i_v \\ \nabla \cdot (-\sigma_{el}^{eff} \nabla \phi_{el(i)}) &= i_v \end{aligned} \tag{3.59}$$

Boundary conditions for ion transport

1. Electrical insulation (i.e no ionic flux) at the electrode/channel interface and at the walls of the electrode.

$$\begin{aligned} \mathbf{n} \cdot \mathbf{i_v}|_{\partial\Omega_{wall}} &= 0 \\ \mathbf{n} \cdot \mathbf{i_v}|_{\partial\Omega_{electrode/channel}} &= 0 \end{aligned} \tag{3.60}$$

2. For the half-cell model, an ideal cathode boundary condition is implemented at the electrolyte/cathode interface. The ideal cathode boundary condition assumes that all losses associated with the cathode are negligible and that $\Delta\phi_{ed(c)} = \Delta^{eq}_{\phi_{ed(c)}}$.

$$\begin{aligned} \Delta\phi_{ed(c)} &= \Delta^{eq}_{\phi_{ed(c)}} \\ \phi_{ed(c)}|_{\partial\Omega_{cathode/electrolyte}} &= V_c - \Delta^{eq}_{\phi_{ed(c)}} \end{aligned} \tag{3.61}$$

where V_c is the electric potential at the cathode/channel interface.

Boundary conditions for electron transport

1. Electrical insulation (i.e no electronic flux) at the walls of the electrode and at the electrode/electrolyte interface.

$$\begin{aligned} \mathbf{n} \cdot \mathbf{i_v}|_{\partial\Omega_{wall}} &= 0 \\ \mathbf{n} \cdot \mathbf{i_v}|_{\partial\Omega_{electrode/electrolyte}} &= 0 \end{aligned} \tag{3.62}$$

2. An anode reference potential is imposed at the anode/channel interface and an electric potential boundary condition, V_c is imposed at the cathode/channel interface (for the full-cell model)

$$\begin{aligned} \phi_{ed(a)}|_{\partial\Omega_{anode/channel}} &= 0 \\ \phi_{ed(c)}|_{\partial\Omega_{cathode/channel}} &= V_c \end{aligned} \tag{3.63}$$

3.5 Input parameters and base case conditions

This section will summarize how input parameters, which are required for the solution of the multiphysics model presented in the previous section, are obtained or calculated. Our base case model is a Ni-infiltrated YSZ supported SOFC anode.

Gas phase transport and thermodynamic properties

The gas phase transport input parameters needed include fuel and air density, viscosities and diffusion coefficients. All gas phase transport properties are calculated using equations derived from the kinetic theory of gases (Hirschfelder *et al.*, 1954) and the gas phase thermodynamic properties, such as reaction enthalpies, entropies and Gibbs free energies are calculated as functions of temperature using the from JANAF thermochemical tables (Chase *et al.*, 1985).

Input parameters to calculate exchange current density

To calculate the exchange current density of the anode and the cathode, the variables defining p^*_{H2} and p^*_{O2} needs to be specified. Table [3.1] defines the necessary variables that

is needed to calculate the exchange current density.

Table 3.1: Variables necessary to calculate the exchange current density as defined in Zhu *et al.* (2005)

Parameter	Description	Numerical Value
A_{des}	Pre-exponential factor for the H_2 desorption reaction	$5.59 \times 10^{19}\ s.cm^2/mol$
E_{des}	Activation energy for the H_2 desorption reaction	$88.12\ kJ/mol$
Γ	Surface site density of Ni	$2.6 \times 10^{-9}\ mol/cm^2$
A_{O2}	Pre-exponential factor for the O_2 desorption reaction on LSM	$4.9 \times 10^{8}\ atm$
E_{O2}	Activation energy for the oxygen desorption reaction on LSM	$200\ kJ/mol$

Parameters required to compute effective conductivity and active TPB length for Ni-infiltrated anode and composite electrodes

The input parameters required to calculate effective electronic conductivity and active TPB length for an infiltrated Ni anode, for a composite Ni-YSZ anode, composite LSM-YSZ cathode and the functional layer of the Ni-infiltrated "bi-layer" porous YSZ anode are summarized in Table [3.2], Table [3.3] and Table [3.4] respectively.

Table 3.2: Model parameters used to calculate effective properties for an infiltrated Ni anode

Parameter	Description	Numerical Value
ϕ_{open}	Open porosity of porous substrate	0.43
V_{YSZ}	YSZ Volume fraction	0.57
R_{YSZ}	Radius of YSZ particles	$0.5 \times 10^{-6} m$
r_{Ni}	Radius of Ni particles	$50 \times 10^{-9} m$
V_{Ni}^{ref}	Reference Ni volume fraction	0.155
σ_{ref}	Reference effective conductivity	716.71 $\frac{S}{cm}$
V_{Ni}^{c}	Critical Ni volume fraction	0.075

Table 3.3: Model parameters used to calculate effective properties for an composite Ni-YSZ anode and composite LSM-YSZ cathode

Parameter	Description	Numerical Value
	Anode	
ϕ_{anode}	Porosity of composite anode	0.35
V_{Ni}	Ni Volume fraction	0.23
V_{YSZ}	YSZ volume fraction	0.42
R_{YSZ}	Radius of YSZ particles	$0.5 \times 10^{-6} m$
r_{Ni}	Radius of Ni particles	$0.5 \times 10^{-6} m$
	Cathode	
$\phi_{cathode}$	Porosity of cathode	0.35
V_{LSM}	LSM Volume fraction	0.315
V_{YSZ}	YSZ Volume fraction	0.335
R_{YSZ}	Radius of YSZ particles	$0.5 \times 10^{-6} m$
r_{LSM}	Radius of LSM particles	$0.5 \times 10^{-6} m$

Table 3.4: Model parameters used to calculate effective properties for a composite Ni-YSZ functional layer of Ni-infiltrated "bi-layer" cell.

Parameter	Description	Numerical Value
	Anode	
ϕ_{anode}	Porosity of composite functional anode	0.19
V_{Ni}	Ni Volume fraction	0.375
V_{YSZ}	YSZ volume fraction	0.375
R_{YSZ}	Radius of YSZ particles	$0.5 \times 10^{-6} m$
r_{Ni}	Radius of Ni particles	$0.5 \times 10^{-6} m$

Summary of effective electric and ionic conductivity and active TPB for composite electrodes

The microstructural composition of the composite anode support layer and cathode used in the model is fixed as listed in Table [3.3]. The effective conductivity and active TPB length for a composite Ni-YSZ anode and LSM-YSZ cathode is summarized in Table [3.5]. The

Table 3.5: Effective properties of a composite Ni-YSZ anode and LSM-YSZ cathode

Parameter	Description	Numerical Value
	Anode	
λ^a_{comp}	Active TPB length ($^m/_{m^2}$)	8.8×10^{11}
$\sigma^a_{el,comp}$	Effective electrical conductivity ($^S/_{cm}$)	25.68
$\sigma^a_{ion,comp}$	Effective ionic conductivity ($^S/_{cm}$)	0.0023
	Cathode	
λ^c_{comp}	Active TPB length ($^m/_{m^2}$)	1.29×10^{12}
$\sigma^c_{el,comp}$	Effective electrical conductivity ($^S/_{cm}$)	3.71
$\sigma^c_{ion,comp}$	Effective ionic conductivity ($^S/_{cm}$)	0.00086

microstructural composition of the composite Ni-YSZ functional layer of the Ni-infiltrated "bi-layer" cell used in the model is fixed as specified in Table [3.4]. The effective electric and ionic conductivity of the composite Ni-YSZ functional layer of the Ni-infiltrated "bi-layer" cell is summarized in Table [3.6].

Table 3.6: Effective properties of a composite Ni-YSZ functional layer of the Ni-infiltrated "bi-layer" cell

Parameter	Description	Numerical Value
	Functional Anode	
λ^a_{comp}	Active TPB length ($^m/_{m^2}$)	7.8587×10^{11}
$\sigma^a_{el,comp}$	Effective electrical conductivity ($^S/_{cm}$)	14.44
$\sigma^a_{ion,comp}$	Effective ionic conductivity ($^S/_{cm}$)	6.1×10^{-3}

Summary of simulation conditions used in the porous anode model

The operating conditions specified in the porous anode model is summarized in Table [3.7]. The mean inlet fuel and air velocities are calculated based on a target current density

Table 3.7: Simulation conditions used in the porous anode model

Parameter	Value
H_2 inlet mole fraction, $x_{H2,in}$	0.97
H_2O inlet mole fraction, $x_{H2O,in}$	0.03
O_2 inlet mole fraction, $x_{O2,in}$	0.21
N_2 mole fraction, $x_{N2,in}$	0.79
Operating temperature, T	1073K
Mean inlet fuel velocity, $V_{fuel,inlet}$	$1.28\frac{m}{s}$
Mean inlet air velocity, $V_{air,inlet}$	$2.98\frac{m}{s}$

generation and 50% fuel and air utilization respectively. The detailed calculations are presented in Appendix E. The inlet mole fractions for the anode were chosen for a hydrogen stream fully humidified at 25^0C. We use a Ni-infiltrated YSZ-porous electrode whose Ni volume fraction correspond to its maximum TPB, given the parameters listed in Table [3.2] and Table [3.8] as a base case to establish mesh independence and to verify that the solution of the model is physically meaningful.

Table 3.8: Model parameters used for base case studies

	Ni volume fraction	Porosity	Effective electrical conductivity, σ_{eff}^{infil} (S/cm)	TPB length, λ_{infil} (m/m^3)
Base case	0.0763	0.354	1.938	2.041×10^{13}

3.6 Solution method

We use COMSOL Multiphysics to solve the 2D porous anode models. COMSOL Multiphysics is a commercial finite element method based modelling package that solves partial differential equations or ordinary differential equations. In the COMSOL framework, we utilize its PARDISO direct solver package to solve the partial differential equations of the governing equations for our 2D porous anode model. We use a quadrilateral mesh for the model geometry and the mesh distribution is controlled by specifying the number of grid points at the boundaries of the electrode. The mesh distribution for the model is shown in Figure 3.3. At the electrode/electrolyte interface, a finer mesh has been employed to ensure that the solver is able to resolve the high gradients associated with the region where most of the electrochemical reactions will occur. We use our base case model to establish mesh independence. This is done by validating the conservation of mass and fluxes of the gas-phase species in the cell. Grid independence of the results was insured by comparing the base case model output for the mass conservation at an anode potential of 0.9V against a mesh 1.5 times denser and comparing a cross-sectional hydrogen concentration profile near the fuel channel inlet. Anode potential refers to the nominal overpotential of the anode. The comparison of the hydrogen concentration profile for the two different mesh profiles is presented in Figure 3.4. The relative difference in the hydrogen concentration profile was of the order of 10^{-6} between the mesh used in our work (with 28160 elements) and a denser mesh of 43800 elements. Each case study that is presented was verified for total

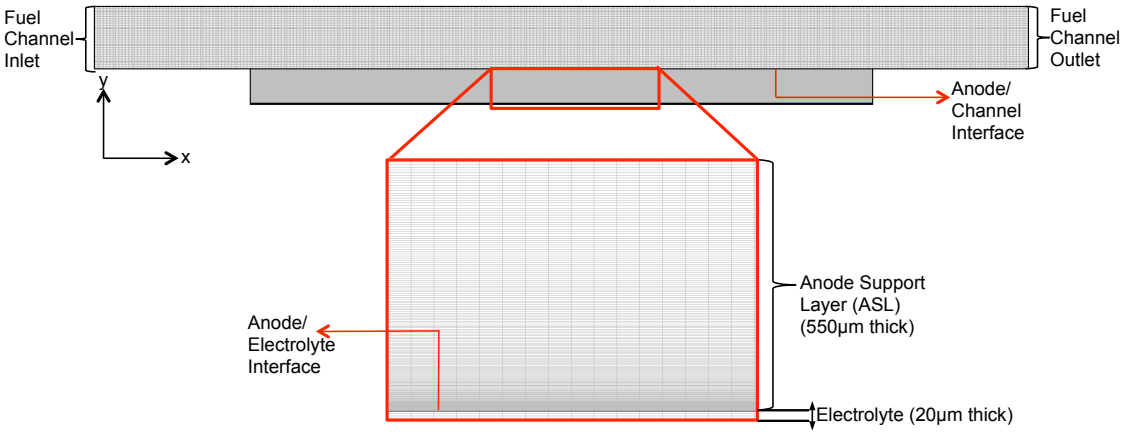

Figure 3.3: Mesh distribution for the anode geometry described in Figure 3.2(a).

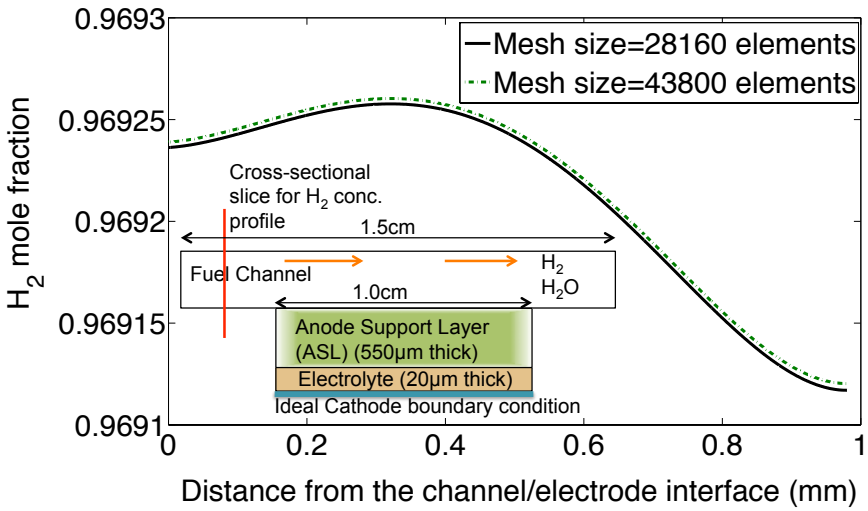

Figure 3.4: Comparison of H_2 concentration profile near the fuel inlet between a coarse mesh of 28160 elements and a finer mesh of 43800 elements. On the x-axis of the concentration profile, $x = 0mm$, represents the top of the fuel channel and $x = 1mm$ represents the bottom of the fuel channel. The concentration profile is generated at constant anode potential of 0.9V. Anode potential refers to the nominal overpotential of the anode. Simulation conditions are outlined in Tables [3.2], [3.7] and [3.8].

mass conservation as well as species conservation.

3.7 Results and Discussion

We utilize the coupled multiphysics model described in the previous sections to determine the relative electrochemical performance of a Ni-infiltrated YSZ supported SOFC when compared against conventional composite Ni-YSZ SOFC. We investigate the effects of Nickel loading on the performance of a planar cell and gain insight on the impact of having an infiltrated support layer on the distribution of electrical potential and hydrogen distribution.

3.7.1 Ni-infiltrated YSZ supported SOFC

The porous anode model predictions depend on a number of factors. Operating conditions such as p_{H2}, p_{H2O}, total pressure and temperature will affect electrochemical kinetics and some of the transport properties. Microstructural parameters of the Ni-infiltrated anodes such as porosity and Ni-connectivity will affect effective properties of the electrode. Here, we discuss/examine the effect of microstructural parameters on Ni-YSZ anode performance.

The first set of results we present is the effect of Ni loading for the infiltrated Ni-YSZ support layer on the performance of a planar cell. We utilize effective properties for the infiltrated Ni-YSZ support layer calculated from our semi-continuous film model. Using the model parameters defined in Table [3.2] and the semi-continuous film model equations developed in Chapter 2, we express the effective conductivity and TPB length of the Ni-infiltrated support layer as a function of Ni loading. This is shown in Figure 3.5.

We present cases in which the Ni loading of the Ni-YSZ infiltrated anode is varied to investigate the effects of (1) low Ni loading near the critical Ni volume fraction, (2) Ni loading corresponding to maximum TPB length and (3) maximum Ni loading on the overall performance of the planar cell. We will report how the Ni loading will affect the activation overpotential, the rate at which the hydrogen is consumed and the anode concentration

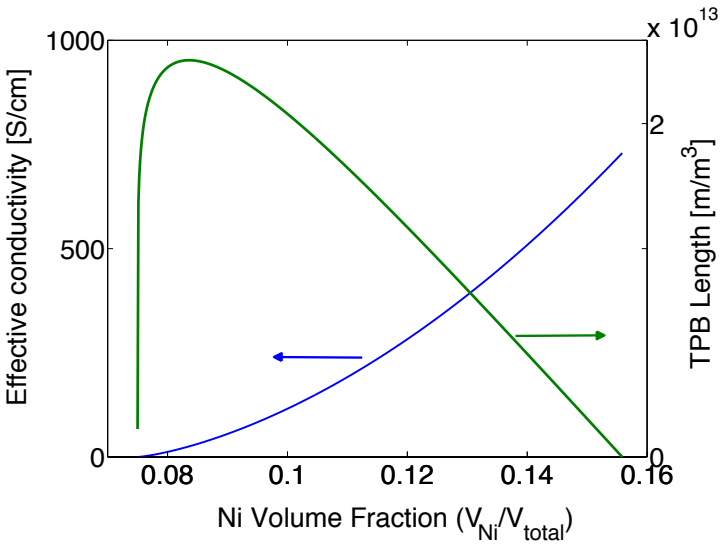

Figure 3.5: Effective conductivity $[S/cm]$ and active TPB length $[m/m^3]$ vs. Ni volume fraction for an infiltrated Ni anode. Effective conductivity and TPB length profiles are generated using semi-continuous film model equations developed in Chapter 2. Model parameters are given in Table [3.2].

overpotential. The anode concentration overpotential, η^a_{conc}, is defined as the loss in cell potential due to the difference in reactant concentration at the reaction sites than the reactant concentration in the bulk region and is represented by Equation 3.64.

$$\eta^a_{conc} = \frac{RT}{2F} \log \left[\frac{x^b_{H2}}{x^b_{H2O}} \cdot \frac{x^r_{H2O}}{x^r_{H2}} \right] \tag{3.64}$$

where x^b_{H2} is the mole fraction of H_2 in the bulk region, x^b_{H2O} is the mole fraction of H_2O in the bulk region, x^r_{H2} is the mole fraction of H_2 at the reaction sites, x^r_{H2O} is the mole fraction of H_2O at the reaction sites. We use the simulation conditions outlined in Table [3.7] and the model parameters for the Ni-YSZ infiltrated anode that varied are summarized in Table [3.9] and the properties of the composite Ni-YSZ anode are defined in Table [3.3].

Ni-infiltrated porous anode polarization curve analysis

From the anode polarization data (Figure 3.6), three distinct characteristics can be

Table 3.9: Model parameters used for case studies to investigate the effects of different Ni loading at the ASL on the electrochemical performance of the cell.

Case studies	Ni volume fraction	Porosity	Effective electrical conductivity, σ_{eff}^{infil} (S/cm)	TPB length, λ_{infil} (m/m^3)
Case a	0.0751	0.365	0.11	1.53×10^{13}
Case b	0.0763	0.354	1.938	2.041×10^{13}
Case c	0.0841	0.346	27.29	2.38×10^{13}
Case d	0.1501	0.280	643.10	2.31×10^{12}

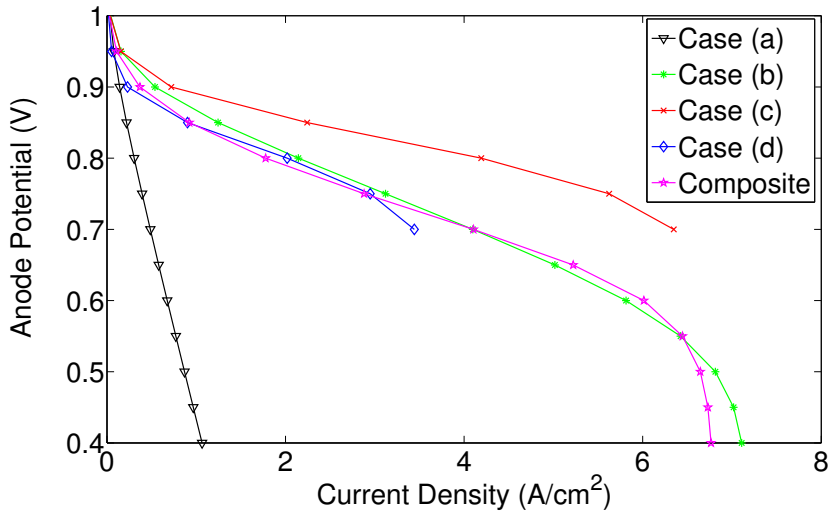

Figure 3.6: Polarization curve of Ni-infiltrated porous YSZ anode with varying Ni loading and with comparison to a composite electrode whose properties are defined in Table [3.3] and Table [3.5]. Anode potential refers to the nominal overpotential of the anode. An ideal dense electrolyte was implemented and an ideal cathode boundary condition imposed at the cathode/electrolyte boundary. Model parameters are given in Tables [3.2], [3.7] and [3.9].

noted with case (a) exhibiting a linear drop in the polarization curve, case(b) showing similar polarization behaviour with the composite electrode even though the Ni-infiltrated cell has a much lower Ni loading when compared to the Ni-YSZ composite cell. The anode performance increases with Ni loading as seen in case (a) to (c) and then decrease with further increase in Ni loading as seen in case (d). This effect can be better appreciated in Figure

3.7. The anode potential reported in Figure 3.6 the refers to the nominal overpotential of the anode.

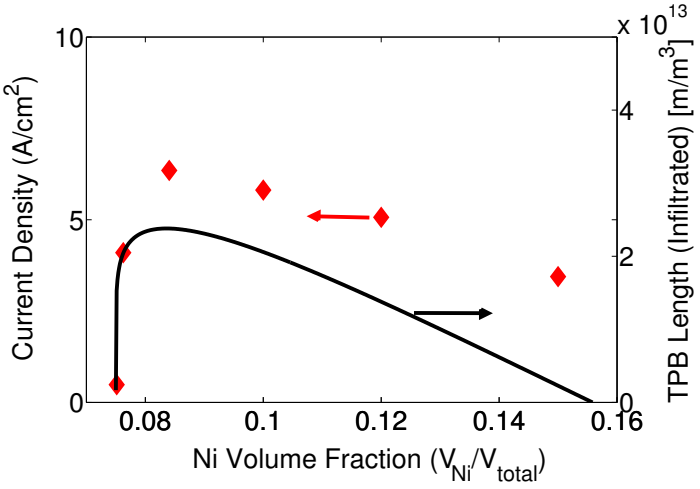

Figure 3.7: Current density and TPB length of Ni-infiltrated cell as a function of Ni loading at a constant anode potential of 0.39V. Anode potential refers to the nominal overpotential of the anode. Model parameters are given in Tables [3.2], [3.7] and [3.9].

From Figure 3.7, it is evident that the current density distribution follows the maxima shape of the TPB curve when plotted against Ni loading.

To investigate the linear drop in the polarization curve for case (a), the effective conductivity of the infiltrated support layer is artificially increased by a factor of 10, while keeping all other parameters constant. The differences in the shape of the polarization curve is shown in Figure 3.8. The polarization curve for the artificially enhanced conductivity case is seen to take the form of a normal polarization curve. Thus proving that the linear drop in polarization curve for case (a) is attributed to the low effective electronic conductivity.

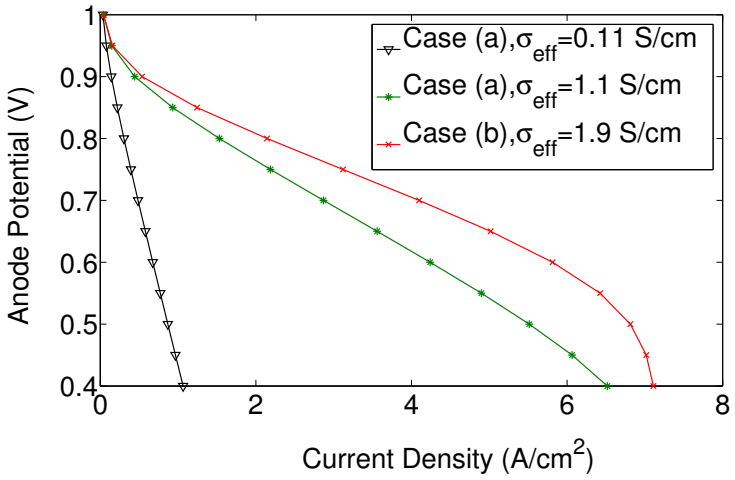

Figure 3.8: Polarization curve of case(a) illustration the effect of artificially increasing the effective conductivity by a factor of 10 with comparison to case (b). Model parameters are given in Tables [3.2], [3.7] and [3.9]. Anode potential refers to the nominal overpotential of the anode.

Ni-infiltrated porous anode overpotential analysis (Constant current density)

In order to gain insight to the effects of the Ni loading on electrochemically active region in the electrode, overpotential profiles at a constant current density of $0.02\frac{A}{cm^2}$. were generated. The activation overpotential (Figure 3.9), H_2 gas reaction rates (Figure 3.10) and concentration overpotential (Figure 3.11) profiles are taken at the middle of the cell as shown in the model geometry and it is a cross-sectional slice from the anode/channel interface to the anode/electrolyte interface.

From the activation overpotential distribution plots (Figure 3.9), the electrochemically active region is confined to within $5\mu m$ from the anode/electrolyte interface for cases (a)-(c). The activation overpotential is also seen to be decreasing from cases(a)-(c). This can be attributed to the increase in both electrical conductivity and TPB length, resulting in lower ohmic resistance and more reaction sites for charge transfer reactions. The activation

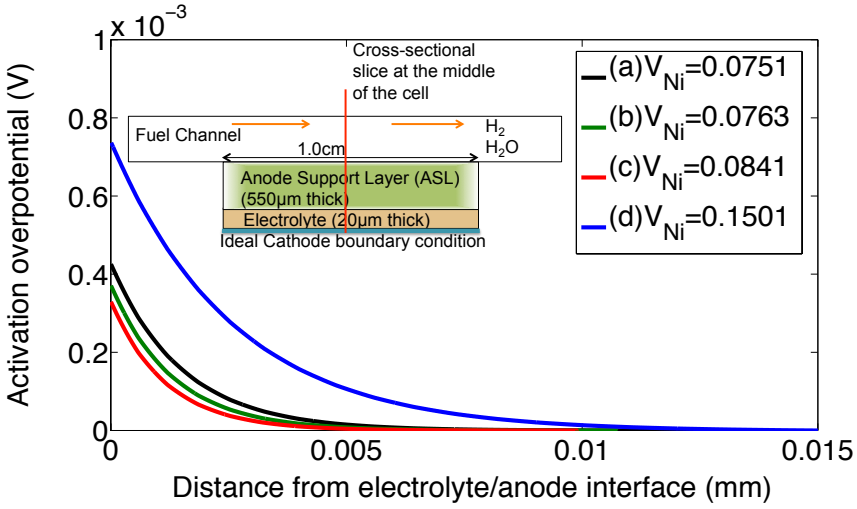

Figure 3.9: Activation overpotential profiles of the 4 cases listed in Table [3.9]. The profiles are extracted from the model via a cross-sectional slice from the anode/channel interface to the anode/electrolyte interface at constant current density of $0.02\frac{A}{cm^2}$. On the x-axis of the concentration profile, $x = 0mm$, represents the electrolyte/anode interface and $x = 0.015mm$ represents the anode/channel interface. Model parameters are given in Tables [3.2], [3.7] and [3.9].

overpotential for case (d) is approximately 2 times higher at the anode/electrolyte interface when compared to cases (a)-(c) and the electrochemically active region is extended to approximately $10\mu m$ from the anode/electrolyte interface. This can be attributed to the significant increase in electric conductivity of the anode without the severe compromise of TPB length with the increased infiltrated Ni loading. In addition, the higher activation overpotential for case (d) can also be explained by considering the Butler-Volmer relationship between current density, exchange current density and activation overpotential.

$$i_v = i_{0,H2}\left[exp\left(\frac{\alpha_a F\eta_{act}}{RT}\right) - exp\left(\frac{-\alpha_c F\eta_{act}}{RT}\right)\right] \tag{3.65}$$

where $i_{0,H2}$ is a linear function of TPB length. With a fixed current density and a fixed bulk phase gas species concentration, an anode with a lower TPB length will require a higher activation overpotential to generate the fixed current density. From Figure 3.10, cases (a)-(c) have comparable consumption rates near the anode/electrolyte boundary with case (a)

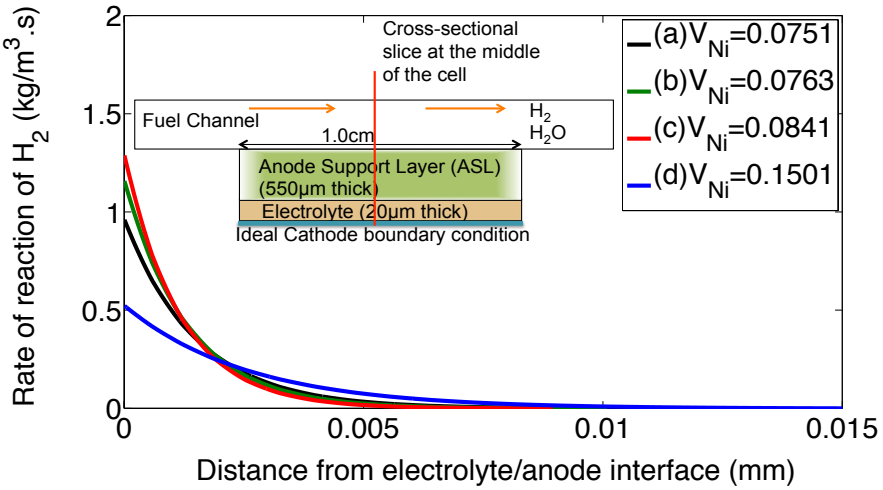

Figure 3.10: $H_2(g)$ reaction profiles of the 4 cases listed in Table [3.9]. The profiles are extracted from the model via a cross-sectional slice from the anode/channel interface to the anode/electrolyte interface at constant current density of $0.02\frac{A}{cm^2}$. On the x-axis of the concentration profile, $x = 0mm$, represents the electrolyte/anode interface and $x = 0.015mm$ represents the anode/channel interface. Model parameters are given in Tables [3.2], [3.7] and [3.9].

having slightly lower H_2 consumption at the anode/electrolyte boundary. An interesting trend to note is that in case (d), H_2 is being consumed along a larger electrochemically active region but consuming a smaller amount of H_2 overall. This can be attributed to a lower amount of active TPB present in high infiltrated Ni loadings despite the high electrical conductivity.

From Figure 3.11, it exemplifies the effect of porosity on the concentration overpotential profiles. The concentration overpotential is seen to be increasing with decreasing porosity with the highest concentration overpotential linked to case (d), which has the lowest porosity.

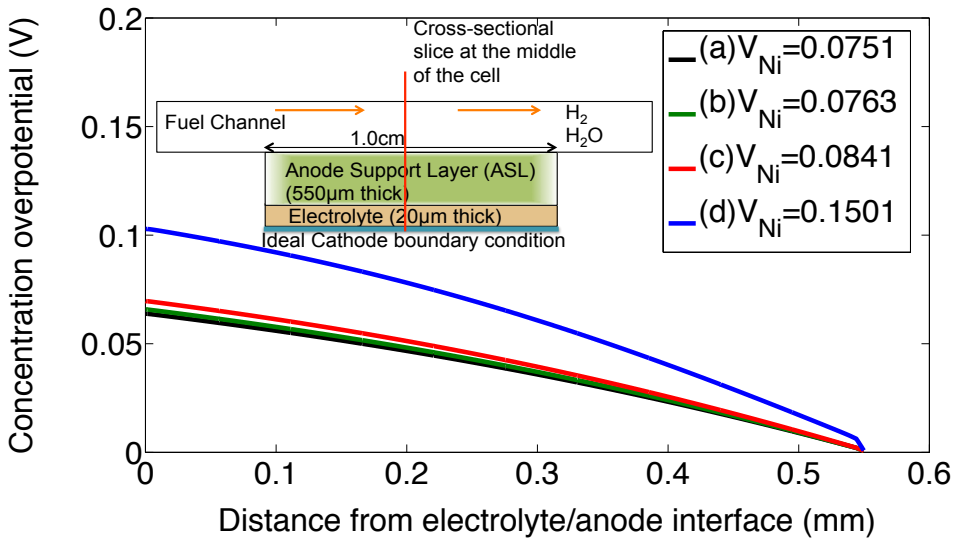

Figure 3.11: Concentration overpotential of the 4 cases listed in Table 3.9. The profiles are extracted from the model via a cross-sectional slice from the anode/channel interface to the anode/electrolyte interface at constant current density of $0.02\frac{A}{cm^2}$. On the x-axis of the concentration profile, $x = 0mm$, represents the electrolyte/anode interface and $x = 0.015mm$ represents the anode/channel interface. Model parameters are given in Tables [3.2], [3.7] and [3.9].

Effect of experimentally controlled parameters

From our semi-continuous film model, it was determined that the pertinent effective properties ($\sigma^{eff}_{Ni(infil)}$, λ^{infil}_{TPB}) are sensitive to the critical Ni volume fraction, V^c_{Ni} and Ni particle sizes, r_{Ni}. We report current density at an anode overpotential of 0.8V to determine the changes in electrochemical performance when the critical Ni volume fraction and Ni particles sizes are varied. The effect of experimentally controlled parameters simulation was carried out at constant V_{Ni}=0.09. The corresponding changes to $\sigma^{eff}_{Ni(infil)}$, λ^{infil}_{TPB} when V^c_{Ni} and r_{Ni} are varied are presented in Table [3.10].

We use the Ni-infiltrated microstructural parameters that correspond to the maximum TPB length as from the analysis of the cell performance data, having a Ni volume fraction that corresponds to the maximum in TPB length provides the best performance.

Table 3.10: Effective properties of infiltrated anode as a function of experimentally controlled parameters. The effect of experimentally controlled parameters simulation was carried out at constant V_{Ni}=0.09.

Experimental Parameter (r_{Ni})	Effective electrical conductivity, σ_{eff}^{infil} (S/cm)	TPB length, λ_{infil} (m/m^3)
50 nm	27.29	2.38×10^{13}
75nm	27.29	1.586×10^{13}
100nm	27.29	1.19×10^{13}
Experimental Parameter (V_{Ni}^c)	**Effective electrical conductivity, σ_{eff}^{infil} (S/cm)**	**TPB length, λ_{infil} (m/m^3)**
0.06	114.4	2.0×10^{13}
0.07	76.29	2.213×10^{13}
0.08	34.63	2.373×10^{13}

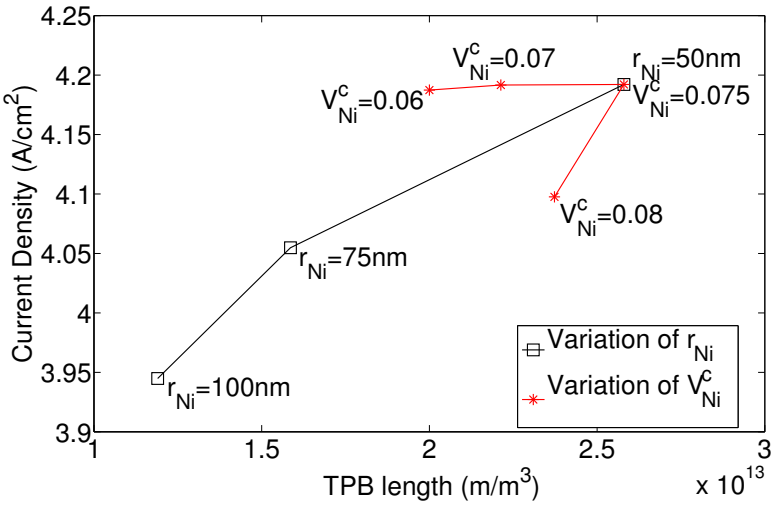

Figure 3.12: Current density versus TPB length plots for varying r_{Ni} (constant V_{Ni}^c=0.075) and varying V_{Ni}^c (constant r_{Ni}=50nm). The current density reported corresponds to an anode potential of 0.8V. Anode potential refers to the nominal overpotential of the anode. Simulation parameters are given in Table [3.10], Table [3.2] and [3.7].

From Figure 3.12, it can be observed that a smaller Ni particle size, yielding a higher TPB length, results in higher current density being generated. However, from the variation

of critical Ni volume fraction, it can be seen that there are two competing effects, effective electrical conductivity and active TPB length, dictating the performance of the anode. This is evident when the cases of V_{Ni}^{c} of 0.07 and 0.08 are compared. While $V_{Ni}^{c} = 0.08$ has a higher TPB length compared to the case where $V_{Ni}^{c} = 0.07$, its lower electrical conductivity compared to the case where $V_{Ni}^{c} = 0.08$ limits its current density output.

3.7.2 Ni-infiltrated "bi-layer" YSZ supported SOFC anode

The Ni-infiltrated "bi-layer" YSZ supported SOFC anode consists of a Ni-infiltrated support layer and a composite Ni-YSZ functional layer. This is in accordance with the cells that are fabricated at University of Calgary. From the analysis of the Ni-infiltrated porous anode model, it was concluded that the optimal Ni loading should be corresponded to the maximum TPB length as it provides the highest number of reaction sites and does not compromise the electrical conduction pathway. Drawing from that conclusion, we use the Ni-infiltrated microstructural parameters that correspond to the maximum TPB length as input parameters to the Ni-infiltrated support layer. The composition of the Ni-YSZ functional layer are given in Table [3.4].

Ni-infiltrated "bi-layer" YSZ anode polarization curve analysis

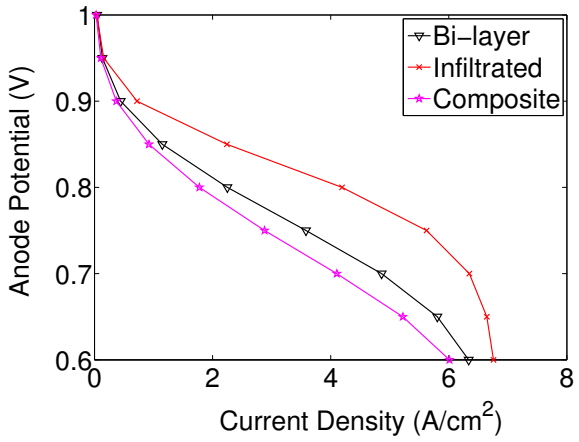

Figure 3.13: Polarization curve of Ni-infiltrated porous YSZ anode, composite Ni-YSZ anode and a Ni-infiltrated "bi-layer" anode. Anode potential refers to the nominal overpotential of the anode. An ideal dense electrolyte was implemented and an ideal cathode boundary condition imposed at the cathode/electrolyte boundary. Model parameters are given in Tables [3.2], [3.4], [3.7] and [3.9].

From the polarization curve, it is evident that the Ni-infiltrated only anode performs better than the bi-layer cell. However, the bi-layer cell performs better than the conventional

composite electrode. This re-emphasizes that the TPB length plays a more significant role in dictating the performance of the cell when there is sufficient electrical conductivity of the Ni phase. We perform a deeper analysis in comparing the performance results between the Ni-infiltrated only anode and the "bi-layer" anode. From Figure 3.14, it is evident that

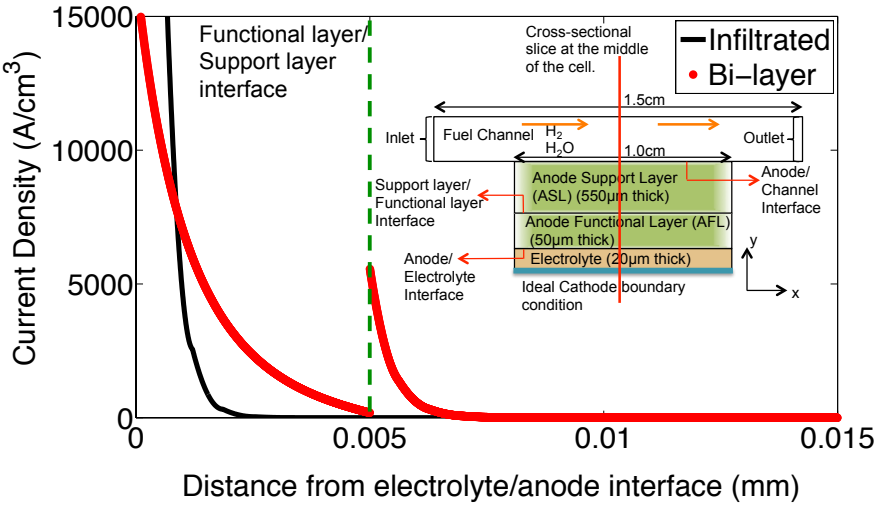

Figure 3.14: Current density profile of Ni-infiltrated "bilayer" anode compared against a Ni-infiltrated electrode. Current density profile is extracted from the model via a cross-sectional slice from the anode/channel interface to the anode/electrolyte interface at an anode potential of 0.8V. Anode potential refers to the nominal overpotential of the anode. Model parameters are given in Tables [3.2], [3.4], [3.7] and [3.9].

there are two sources of current contributions in the bi-layer cell. One contribution is from the composite functional layer and the other is from the infiltrated support layer. There is a discontinuity in the current density profile and this takes place at the interface between the composite functional layer and the infiltrated support layer. This can be explained by considering the sudden change in effective properties from the infiltrated support layer and the composite functional layer summarized in Table [3.11]. The sharp jump in current density occurs due to the sharp contrast of the active TPB length at the infiltrated support layer and the composite functional layer. Physically, the sharp change in effective properties

Table 3.11: Effective properties of a composite functional layer and the Ni-infiltrated support layer of the Ni-infiltrated "bi-layer" anode

Parameter	Description	Numerical Value
	Functional anode layer	
λ^{a}_{comp}	Active TPB length ($^{m}/_{m^2}$)	7.8587×10^{11}
$\sigma^{a}_{el,comp}$	Effective electrical conductivity ($^{S}/_{cm}$)	14.44
	Infiltrated support layer	
λ_{infil}	Active TPB length(m/m^3)	2.38×10^{13}
σ^{infil}_{eff}	Effective electrical conductivity ($^{S}/_{cm}$)	27.29

in the "bilayer" anode does not occur. From a fabrication point of view, there will be a gradual microstructural change between the infiltrated support layer and the composite support layer, which should result in a smooth current density curve decreasing from the anode/electrolyte interface towards the anode/gas channel interface, similar to how the current density profile of the Ni-infiltrated anode looks like.

3.7.3 Full cell model analysis

The cathodic and dense electrolyte losses are added to the anode polarization model, which allows us to analyze the effect of pure Ni- infiltration anode versus a "bi-layer" anode manufacturing technique from a full SOFC cell perspective. The polarization curve of the Ni-infiltrated anode is compared against the polarization curve of the "bi-layer" anode and is presented in Figure 3.15. We utilized the Ni-infiltrated microstructural parameters that correspond to the maximum TPB length as input parameters to the Ni-infiltrated support layer. The simulation conditions are specified in Tables [3.2], [3.5], [3.6] and [3.7].

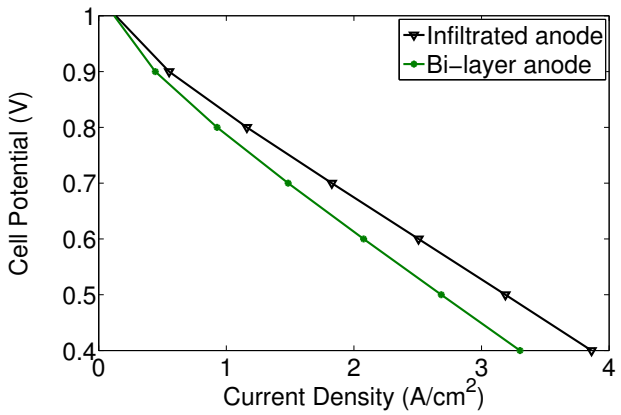

Figure 3.15: Polarization curve comparing the effect of pure Ni-anode infiltration versus a "bi-layer" anode manufacturing technique from a full SOFC cell perspective. Model parameters are given in Tables [3.2], [3.5], [3.6] and [3.7].

With the addition of the cathodic and dense electrolyte losses, it is still evident that the pure Ni-infiltration anode performs better than the "bi-layer" anode manufacturing technique.

3.8 Conclusion

A 2D porous anode model that considers the coupled effect of detailed electrochemistry, gas-phase transport phenomena in the bulk diffusion regime as well as in porous media has been developed to examine the effect of experimentally controllable variables such as Ni loading and porosity on the electrochemical performance of Ni-infiltrated SOFC anodes. The results of the anode performance model indicate that the maximum performance is correlated to a Ni-loading corresponding to the maximum in TPB. It is demonstrated that the Ni-infiltrated porous electrode can achieve comparable performance to the conventional composite electrode but at a much lower Ni loading. We have also compared the electrochemical performance of a Ni-infiltrated only anode to Ni-infiltrated "bi-layer" YSZ supported SOFC anode that consists of a Ni-infiltrated support layer and a composite Ni-YSZ functional layer. The Ni-infiltrated only anode is still superior in performance compared to the bi-layer cell. However, the bi-layer cell performs better than the conventional composite electrode.

To validate the electrochemical anode performance data, a consistent set of experimental data for button cells with homogeneous microstructural properties need to be collected. The 2D porous anode model geometry can be modified to match the experimental cell and correlate the polarization resistance measured in impedance with overpotential and current density relationship predicted by the anode model.

Chapter 4

Conclusion and Recommendations

4.1 Conclusion

A novel semi-continuous film model based on percolation theory has been developed to describe Ni-infiltrated SOFC anodes. Specifically, the model relates the effective conductivity and triple phase boundary (TPB) as a function of experimentally controlled parameters such as Ni loading and porosity. This model is the first of its kind to correlate the semi-continuous film morphology of infiltrated Ni to pertinent effective properties of SOFC electrodes, which conventionally have been made of and described in terms of mixtures of two types of particles. From the semi-continuous film model, it was determined that there is an optimal Ni loading for a Ni-infiltrated SOFC anode corresponding with the maximum in the TPB length. Too little Ni results in non-percolating Ni-phase whereas too much Ni impregnation causes reduced number of reaction sites as the Ni covers more of the porous YSZ surface. At a Ni loading, V_{Ni} near the critical Ni loading, V_{Ni}^c, such as $V_{Ni} = 0.076$ with a corresponding $V_{Ni}^c = 0.075$, a largely disconnected Ni network results in both a low number of active reaction sites and a low effective electrical conductivity, $\sigma_{eff} = 1.4\frac{S}{cm}$.

A 2D porous anode model has been developed to examine the effect of experimentally controllable variables such as Ni loading and porosity on the electrochemical performance of

Ni-infiltrated SOFC anodes. The driving force of this work is two-fold (i) to guide the anode design by identifying the electrode parameters such as Ni loading and porosity that maximize anode electrochemical performance (ii) to provide a theoretical basis/interpretation of experimental data. Key input parameters such as the effective conductivity and active TPB length of the Ni-infiltrated anodes were calculated from the semi-continuous film model I developed. The results of the anode performance model indicate that the maximum performance is correlated to a Ni-loading corresponding to the maximum TPB. It was demonstrated that the Ni-infiltrated porous electrode can achieve comparable performance to the conventional composite electrode. An infiltrated anode with a Ni loading, $V_{Ni} = 0.076$ generates $3.12\frac{A}{cm^2}$ of current at an nominal anode overpotential of 0.75V, compared to a composite Ni-YSZ anode with a Ni loading, $V_{Ni} = 0.23$, generates $2.89\frac{A}{cm^2}$ of current at an nominal anode overpotential of 0.75V.

4.2 Recommendations

In developing the semi-continuous film model, it is identified that the film thickness growth mechanism has a significant impact on the effective properties of the semi-continuous Ni film. The mechanism of film growth with increasing Ni loading could be experimentally determined and this can be done by examining SEM images at progressive stages of Ni-infiltration to correlate thickness of the film with Ni loading. In addition, experimental conductivity measurements for an infiltrated electrode as a function of Ni loading can be carried out to verify the trends observed by the semi-continuous film model developed.

To validate the electrochemical anode performance predictions, a consistent set of experimental data for button cells with homogeneous microstructural properties needs to be collected. The 2D porous anode model geometry can be adjusted to match the experimental cell geometrical dimensions and correlate the polarization resistance measured in impedance with overpotential and current density relationship predicted by the anode model. A mass

transport study can also be carried out to verify if mass transport is an issue due to the high concentration overpotentials observed in the 2D porous anode model. This can be achieved by using different mixture of fuel and inert gases with different diffusivities flowing through the electrode. In addition, the Knudsen effects in the porous electrodes have been approximated using the averaged Bosanquet equation. As a further improvement to the model, it is recommended that a more robust treatment of the combined Knudsen and bulk diffusion developed by Weber and Newman (2005) be adopted. It differs from the commonly used dusty gas model in that the total flux of the gas species is not a linear combination of the diffusive flux and the viscous flux (Weber and Newman, 2005).

References

Abbaspour, A; Luo, J, and Nandakumar, K. Three-dimensional random resistor-network model for solid oxide fuel cell composite electrodes. *Electrochimica Acta*, 55(12):3944 – 3950, 2010.

Atkins, P and De Paula, J. *Physical Chemistry*. Oxford University Press, 2006.

Aziz, M. Film growth mechanisms in pulsed laser deposition. *Applied Physics A: Materials Science and Processing*, 93:579–587, 2008.

Berson, A; Choi, H.-W, and Pharoah, J. G. Determination of the effective gas diffusivity of a porous composite medium from the three-dimensional reconstruction of its microstructure. *Phys. Rev. E*, 83, 2011.

Bessler, W. G; Warnatz, J, and Goodwin, D. G. The influence of equilibrium potential on the hydrogen oxidation kinetics of SOFC anodes. *Solid State Ionics*, 177(39–40):3371 – 3383, 2007.

Bird, R. B; Stewart, W. E, and Lightfoot, E. N. *Transport Phenomena, Revised 2nd Edition*. John Wiley & Sons, Inc., 2nd edition, 2006.

Boragno, C; Buatier de Mongeot, F; Felici, R, and Robinson, I. K. Critical thickness for the agglomeration of thin metal films. *Phys. Rev. B*, 79(15):155443, Apr 2009.

Bouvard, D and Lange, F. Relation between percolation and particle coordination in binary powder mixtures. *Acta Metallurgica et Materialia*, 39(12):3083 – 3090, 1991.

Brodkey, R. S and Hershey, H. C. *Transport Phenomena: A Unified Approach*. Brodkey Publishing, 1988.

Bunde, A and Kantelhardt, J. W. Diffusion and conduction in percolation systems. In Heitjans, P and Kärger, J, editors, *Diffusion in Condensed Matter*. Springer Berlin Heidelberg, 2005.

Busawon, A; Sarantaridis, D, and Atkinson, A. Ni Infiltration as a Possible Solution to the Redox Problem of SOFC Anodes. *Electrochemical and Solid-State Letters*, 11(10): B186–B189, 2008.

Chase, W; Davies, C; Downey, J, and Frurip, D. JANAF Thermochemical Tables, 3rd edition. *Journal of Physical and Chemical Reference Data*, 14(1), 1985.

de Boer, B. *SOFC anode: Hydrogen Oxidation at Porous Nickel and Nickel/Zirconia electrodes*. PhD thesis, Universiteit Twente, Enschede, October 1998.

Gadkari, P. R; Warren, A. P; Todi, R. M; Petrova, R. V, and Coffey, K. R. Comparison of the agglomeration behavior of thin metallic films on SiO2. *Journal of Vacuum Science and Technology A*, 23(4):1152–1161, 2005.

Goodwin, D. G; Zhu, H; Colclasure, A. M, and Kee, R. J. Modeling Electrochemical Oxidation of Hydrogen on Ni-YSZ Pattern Anodes. *Journal of The Electrochemical Society*, 156(9):B1004–B1021, 2009.

Gorte, R and Vohs, J. Nanostructured anodes for solid oxide fuel cells. *Current Opinion in Colloid and Interface Science*, 14(4):236 – 244, 2009.

Grovenor, C; Hentzell, H, and Smith, D. The development of grain structure during growth of metallic films. *Acta Metallurgica*, 32(5):773 – 781, 1984.

Hardjo, E; Monder, D. S, and Karan, K. Numerical Modeling of Nickel-Impregnated Porous YSZ-Supported Anodes and Comparison to Conventional Composite Ni-YSZ Electrodes. *ECS Transactions*, 35(1):1823–1832, 2011.

Hirschfelder, J. O; Curtiss, C. F, and Bird, R. B. *Molecular Theory of Gases and Liquids*. Wiley, 1954.

Jiang, S. P. A review of wet impregnation: An alternative method for the fabrication of high performance and nano-structured electrodes of solid oxide fuel cells. *Materials Science and Engineering: A*, 418(1–2):199 – 210, 2006.

Jiang, S; Wang, W, and Zhen, Y. Performance and electrode behaviour of nano-YSZ impregnated nickel anodes used in solid oxide fuel cells. *Journal of Power Sources*, 147 (1–2):1 – 7, 2005.

Kee, R. J; Zhu, H, and Goodwin, D. G. Solid oxide fuel cells with hydrocarbon fuels. *Proceedings of the Combustion Institute*, 30(2):2379 – 2404, 2005.

Kenney, B; Valdmanis, M; Baker, C; Pharoah, J, and Karan, K. Computation of TPB length, surface area and pore size from numerical reconstruction of composite solid oxide fuel cell electrodes. *Journal of Power Sources*, 189(2):1051 – 1059, 2009.

Kerkhof, P. J. A modified Maxwell-Stefan model for transport through inert membranes: the binary friction model. *The Chemical Engineering Journal and the Biochemical Engineering Journal*, 64(3):319 – 343, 1996.

Klemensø, T; Thydén, K; Chen, M, and Wang, H.-J. Stability of Ni-Yttria stabilized Zirconia anodes based on Ni-impregnation. *Journal of Power Sources*, 195(21):7295 – 7301, 2010.

Krishna, R and Wesselingh, J. The Maxwell-Stefan approach to mass transfer. *Chemical Engineering Science*, 52(6):861 – 911, 1997.

Lee, J.-H; Moon, H; Lee, H.-W; Kim, J; Kim, J.-D, and Yoon, K.-H. Quantitative analysis of microstructure and its related electrical property of SOFC anode, Ni-YSZ cermet. *Solid State Ionics*, 148(1–2):15 – 26, 2002.

Maissel, L. I and Glang, R. *Handbook of thin film technology, edited by Leon I. Maissel and Reinhard Glang*. McGraw-Hill New York,, 1970.

Metcalfe, T. C. Three phase boundary length and effective diffusivity in modeled sintered composite solid oxide fuel cell electrodes. Master's thesis, University of British Columbia, 2008.

Petric, A. Ceramic fuel cells: A century of research. *Canadian Ceramics*, 68(3):63–69, 1999.

Sanyal, J; Goldin, G. M; Zhu, H, and Kee, R. J. A particle-based model for predicting the effective conductivities of composite electrodes. *Journal of Power Sources*, 195(19):6671 – 6679, 2010.

Scher, H and Zallen, R. Critical density in percolation processes. *Journal of Chemical Physics*, 53(9):3759–3761, 1970.

Schneider, P. Multicomponent isothermal diffusion and forced flow of gases in capillaries. *Chemical Engineering Science*, 33(10):1311 – 1319, 1978.

Sholklapper, T. Z; Kurokawa, H; Jacobson, C. P; Visco, S. J, and De Jonghe, L. C. Nanostructured solid oxide fuel cell electrodes. *Nano Letters*, 7(7):2136–2141, 2007.

Sholklapper, T. Z; Jacobson, C. P; Visco, S. J, and De Jonghe, L. C. Synthesis of dispersed and contiguous nanoparticles in solid oxide fuel cell electrodes. *Fuel Cells*, 8(5):303–312, 2008.

Singh, A and Krishnan, V. Anode Characterization and SOFC Performance using Ni-YSZ Anodes Formed by Ni Impregnation Methods. *ECS Transactions*, 6(21):25–32, 2008.

Singhal, S and Kendall, K, editors. *High temperature solid oxide fuel cells: fundamentals, design, and applications*. Elsevier, 2003.

Šmilauer, P. Thin metal films and percolation theory. *Contemporary Physics*, 32(2):89–102, 1991.

Stauffer, D and Aharony, A. *Introduction to percolation theory*. Taylor and Francis, 1994.

Tanner, C. W; Fung, K.-Z, and Virkar, A. V. The effect of porous composite electrode structure on solid oxide fuel cell performance. *Journal of The Electrochemical Society*, 144(1):21–30, 1997.

Todd, B. Mass transport in solid oxide fuel cell electrodes. *2nd International Conference on Heat Transfer, Fluid Mechanics and Thermodynamics*, 2003.

Torabi, A; Hanifi, A. R; Etsell, T. H, and Sarkar, P. Effects of porous support microstructure on performance of infiltrated electrodes in solid oxide fuel cells. *Journal of The Electrochemical Society*, 159(2):B201–B210, 2012.

Tsoga, A; Naoumidis, A, and Nikolopoulos, P. Wettability and interfacial reactions in the systems NiYSZ and Ni/Ti-TiO2/YSZ. *Acta Materialia*, 44(9):3679 – 3692, 1996.

Tucker, M. C; Lau, G. Y; Jacobson, C. P; DeJonghe, L. C, and Visco, S. J. Performance of metal-supported SOFCs with infiltrated electrodes. *Journal of Power Sources*, 171(2): 477 – 482, 2007.

Utz, A; Störmer, H; Gerthsen, D; Weber, A, and Ivers-Tiffée, E. Microstructure stability studies of Ni patterned anodes for SOFC. *Solid State Ionics*, 192(1):565 – 570, 2011.

Wang, Q.-Q; Hun, J.-B; Ding, S; Xiong, G.-G, and Tian, D.-C. Percolation characters of sputtered and vaporized semi-continuous silver island films. *Applied Surface Science*, 243 (1-4):329 – 334, 2005.

Weber, A. Z and Newman, J. Modeling gas-phase flow in porous media. *International Communications in Heat and Mass Transfer*, 32(7):855 – 860, 2005.

Wilson, J. R and Barnett, S. A. Solid Oxide Fuel Cell Ni-YSZ Anodes: Effect of Composition on Microstructure and Performance. *Electrochemical and Solid-State Letters*, 11(10): B181–B185, 2008.

Wilson, J. R; Kobsiriphat, W; Mendoza, R; Chen, H.-Y; Hiller, J. M; Miller, D. J; Thornton, K; Voorhees, P. W; Adler, S. B, and Barnett, S. A. Three-dimensional reconstruction of a solid oxide fuel cell anode. *Nat Mater*, 5(7):541–544, 2006.

Yamamuro, S; Sumiyama, K; Hihara, T, and Suzuki, K. Geometrical and electrical percolation in nanometre-sized Co-cluster assemblies. *Journal of Physics: Condensed Matter*, 11(16):3247, 1999.

Zalc, J; Reyes, S, and Iglesia, E. Monte-carlo simulations of surface and gas phase diffusion in complex porous structures. *Chemical Engineering Science*, 58(20):4605–4617, 2003.

Zhu, H and Kee, R. J. Modeling Distributed Charge-Transfer Processes in SOFC Membrane Electrode Assemblies. *Journal of The Electrochemical Society*, 155(7):B715–B729, 2008.

Zhu, H; Kee, R. J; Janardhanan, V. M; Deutschmann, O, and Goodwin, D. G. Modeling elementary heterogeneous chemistry and electrochemistry in solid oxide fuel cells. *Journal of The Electrochemical Society*, 152(12):A2427–A2440, 2005.

Appendix A

SOFC electrochemistry

A.1 Potential steps concept

The electrical potential distributions along the thickness of the SOFC electrodes and electrolytes are described using the concept of potential steps, $\Delta\phi$, that form at the electrode/electrolyte interfaces. $\Delta\phi$ arises due to the electrical double layers that are formed at the electrode/electrolyte interface. The electrical double layers will also form space charge regions of excess electrical charges that will affect the bulk electrode/electrolyte potential difference. However, in our work, we assume that the effects of the surface double layers due to accumulation of charged or partially charged adsorbed species are negligible and $\Delta\phi$ is defined as the difference between the electric phase potential of the electrode, ϕ_{ed} and the electric potential of the electrolyte, ϕ_{el} (Equation [A.1]) (Bessler *et al.*, 2007)

$$\Delta\phi = \phi_{ed} - \phi_{el} \tag{A.1}$$

During a charge-transfer reaction taking place at the electrical double layers, electrons are transferred between a delocalized conduction-band state within the metal electrode and a localized molecular orbital of a charged species on the electrolyte. This is described using potential-energy surfaces schematic in Figure A.1 adopted from the work of Kee *et al.* (2005)

The left pane in Figure A.1 represents the atomic configurations of the hydrogen atom on the

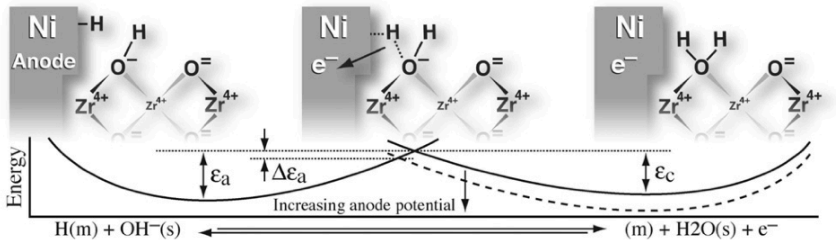

Figure A.1: Potential-energy surface schematic of a charge transfer reaction (Reaction [3.3]) adopted from Kee *et al.* (2005)

Nickel metal and the oxygen ion at the YSZ surface before charge transfer, the central pane represents the transition state of the charge transfer reaction and the right pane represents the product atomic configurations after the charge transfer reaction. The reactant needs to overcome the activation barrier, ϵ_a before proceeding the forward direction of the charge transfer and similarly, the product will need to overcome its own activation barrier, ϵ_c before proceeding in the reverse direction of the charge transfer. Assuming that both the reactant and product have Boltzmann energy distributions, the forward and reverse rates of the charge transfer reaction will be of the form described in Reaction 3.3. When the cell is polarized, the energy profiles of the two potential surfaces will shift relative to one another and the activation energies will shift accordingly. The shift in the energy profiles of the two potential surfaces is captured via the activation overpotential, η_{act}. The activation overpotential describes the deviation of the energy profiles of the two potential surfaces away from its equilibrium energy profile and is expressed in equation [A.2].

$$\eta_{act} = \Delta\phi - \Delta\phi_{eq} \tag{A.2}$$

where $\Delta\phi_{eq}$ is the local equilibrium phase potential. The activation overpotential, as defined, will then be used in a Butler-Volmer like equation developed by Zhu *et al.* (2005) expressed in equation [A.3] to correlate the current density, i_V to the electric potentials,

surface coverages and gas phase species.

$$i_v = i_{0,H2}\left[exp\left(\frac{\alpha_a F\eta_{act}}{RT}\right) - exp\left(\frac{-\alpha_c F\eta_{act}}{RT}\right)\right] \tag{A.3}$$

where η_{act} is the local activation overpotential and it is defined in equation [A.2] and $\alpha_{a,c}$ is the charge transfer coefficient.

A.1.1 Equilibrium potential

The local equilibrium potential is defined by considering the global half-cell reaction:

$$H_2(g) + O^{2-}_{ads,el} \rightleftharpoons H_2O(g) + V_o^{\cdot\cdot}(ads, el) + 2e^-_{ed} \tag{A.4}$$

The local equilibrium potential at the anode ($\Delta\phi^{an}_{eq}$) is then calculated by the Nernst equation:

$$\Delta\phi^{an}_{eq} = \frac{\Delta G^0}{2F} - \frac{RT}{2F} ln \frac{a(H_2)}{a(H_2O)} \frac{a(O^{2-})}{a(V_o^{\cdot\cdot})} \tag{A.5}$$

ΔG^0 is the standard state Gibbs free energy of reaction and is expressed in equation [A.6].

$$\Delta G^0 = \mu^0_{H2O} - \mu^0_{H2} - \mu^0_{O^{2-}} \tag{A.6}$$

In order to remain thermodynamically consistent, we have included the activities of O^{2-} and $V_o^{\cdot\cdot}$ in the calculation of $\Delta\phi^{an}_{eq}$. By convention, the thermodynamic properties of the vacancy is set to zero. However, the thermodynamic properties of O^{2-} is unknown. Theoretically, it can be calculated from the absolute electrical potential between Ni and YSZ. However, the absolute electrical potential cannot be physically measured as it involves the measurement of potential difference between two different solid phases (Goodwin *et al.*, 2009). In order to estimate the standard state thermodynamic property of the bulk phase oxygen ion, we adopt the work of Goodwin et al. (Goodwin *et al.*, 2009), where they have considered the global oxygen-reduction reaction at equilibrium.

$$\frac{1}{2}O_2(g) + V_o^{\cdot\cdot}(ads, el) + 2e^-_{ed} \rightleftharpoons O^{2-}_{ads,el} \tag{A.7}$$

The equilibrium reaction can be expressed as functions of electric potential across LSM and YSZ, E_c, standard state Gibbs free energy, ΔG^0, bulk oxygen vacancy fraction, X_{Vo} and partial pressure of oxygen, p_{O2}. (Equation [A.8])

$$\frac{1 - X_{Vo}}{(p_{O2})^{0.5} X_{Vo}} = exp\left(\frac{-\Delta G^0}{RT}\right) exp\left(\frac{-2FE_c}{RT}\right) \tag{A.8}$$

$$\Delta G^0 = \mu^0_{O^{2-}} - 0.5\mu^0_{O_{2(g)}} - \mu^0_{V_o}$$

Assume the potential difference across the double layer of LSM and YSZ, E_c to be 0.5V and using the convention that the activities of the vacancy is 0, Equation [A.8] can be arranged to solve for $\mu^0_{O^{2-}}$. The activity of O^x_o is assumed to be 1 when the assumption that the YSZ surface is nearly fully covered with O^{2-}. It should be noted that the choice of the numerical value of the potential difference across the double layer does not impact the calculation of the local equilibrium potential as the thermodynamic data of these species cancel out when the two half-cell potential steps are added (Bessler *et al.*, 2007).The standard state chemical potentials of the gaseous species can be calculated from JANAF thermochemical tables (Chase *et al.*, 1985).

A.2 Key variables for Butler-Volmer equation

From the derivation of the modified Butler-Volmer equation, p^*_{H2} is determined by considering the equilibrium reaction of the H_2 adsorption on Ni and expressing the hydrogen surface coverage as a function of K_1 and the partial pressure of H_2.

$$p^*_{H2} = \frac{A_{des}\Gamma\sqrt{2\pi M_{H2}}}{\gamma_0\sqrt{RT}} exp\left(\frac{-E_{des}}{RT}\right) \tag{A.9}$$

The forward reaction rate constant of reaction 3.1 is expressed in terms of a sticking coefficient, γ_0 in Equation [A.10]

$$k_1 = \gamma_0\sqrt{\frac{RT}{2\pi M_{H2}}} \tag{A.10}$$

where M_{H2} is the molecular weight of hydrogen gas and γ_0 is the sticking coefficient associated with the adsorption reaction, which is assumed to be 0.01. The reverse reaction rate constant of reaction 3.1 is expressed in Equation [A.11]

$$k_{-1} = A_{des} exp\left(-\frac{E_{des}}{RT}\right)\Gamma^2\theta_H^2 \tag{A.11}$$

where A_{des} is the pre-exponential factor for the H_2 desorption reaction, E_{des} is the activation energy for the desorption reaction and Γ is the surface site density of Nickel. Using equations [A.10] and [A.11], the parameter p^*_{H2} is defined in equation [A.9].

Appendix B

Derivation of Maxwell-Stefan equations

The spatial distribution of the gas-phase chemical species in the flow channels is modeled using the convection-diffusion equation [B.1].

$$\nabla \cdot \mathbf{j}_i + \rho \mathbf{v} \cdot \nabla \omega_i = R_i \tag{B.1}$$

where $\mathbf{j}_i$ is the diffusive mass flux vector of species i, ω_i is the mass fraction of species i. The convective flux is given by the second term of Equation [B.1]. R_i is the reaction term and since there is no reaction in the flow channels, $R_i = 0$. The diffusive flux is a sum of temperature-dependent driving force and diffusional driving force (Equation [B.2]) as outlined in (Bird *et al.*, 2006).

$$\mathbf{j_i} = (-D_i^T \nabla lnT) - \rho \omega_i \sum_{\substack{j=1 \\ i \neq j}}^{n} \tilde{D}_{ij} \mathbf{d}_j \tag{B.2}$$

In our work, we simplify the diffusive flux and do not consider the temperature dependent driving force. $\tilde{D}_{ij}$ refers to multicomponent Fick diffusivity and it is defined from considering

the composition dependence of the frictional interaction parameter as derived from non-equilibrium thermodynamics (Equation [B.3]).

$$\tilde{D}_{ij} = \frac{-cRT\ddot{a}_{ij}}{\rho_i \rho_j} \tag{B.3}$$

$\ddot{a}_{ij}$ is defined as the frictional interaction parameter and it obeys Onsager reciprocal relations. Thus, $\tilde{D}_{ij}$ will also obeys Onsager reciprocal relations and the symmetry of $\tilde{D}_{ij}$ must be maintained. Considering a binary system of species i and j, $\tilde{D}_{ij}$ is related to the binary diffusion coefficients, D_{ij} (for multicomponent diffusion in gases at low density) via equation [B.4].

$$\begin{aligned} \tilde{D}_{ii} &= -\frac{\omega_j^2}{x_i x_j} D_{ij} \\ \tilde{D}_{jj} &= -\frac{\omega_i^2}{x_i x_j} D_{ij} \\ \tilde{D}_{ij} = \tilde{D}_{ji} &= -\frac{\omega_i \omega_j}{x_i x_j} D_{ij} \end{aligned} \tag{B.4}$$

The binary diffusion coefficients, D_{ij} are determined using the empirical correlation determined by Krishna and Wesselingh (1997).

$$D_{ij} = \frac{3.16 \times 10^{-8} T^{1.75}}{p \left(v_i^{\frac{1}{3}} + v_j^{\frac{1}{3}} \right)^2} \left[\frac{1}{M_i} + \frac{1}{M_j} \right]^{0.5} \tag{B.5}$$

v_i and v_j are molar diffusion volumes. M_i and M_j are the molecular weights of species i and j respectively. The diffusional driving force $\mathbf{d}_j$ as derived by Bird *et al.* (2006) account for the concentration diffusion and pressure diffusion, temperature dependent driving force and forced diffusion. This is expressed in Equation [B.6].

$$cRT\mathbf{d}_j = \nabla x_j + (x_j - \omega_j)\frac{\nabla p}{p} - \rho_j \mathbf{g_j} + \omega_j \sum_{\alpha=1}^{n} \rho_\alpha \mathbf{g}_\alpha \tag{B.6}$$

There is no forced diffusion in the SOFC cell and as such, the forced diffusion term is neglected. The simplified expression is expressed in Equation [B.7]:

$$cRT\mathbf{d}_j = \nabla x_j + (x_j - \omega_j)\frac{\nabla p}{p} \tag{B.7}$$

Substituting Equation [B.7] into Equation [B.2] yields the final implicit form, Equation [B.8], of the Maxwell-Stefan formulation that will be solved in the model.

$$\nabla \cdot \left[\rho \omega_i u \; - \rho_i \sum_{\substack{j=1 \\ i \neq j}}^{n} \tilde{D}_{ij} \left[\nabla x_j + (x_j - \omega_j) \frac{\nabla p}{p} \right] \right] = 0 \tag{B.8}$$

Appendix C

Knudsen diffusion

Knudsen diffusion occurs in porous media when the mean free path length in the gas is larger than the pore sizes of the porous medium. This increases the frequency at which the gas collides with the walls, increasing the effects of the wall surface interactions on the flow characteristics. Knudsen diffusion can be characterized by the Knudsen number, K_n.

$$K_n = \frac{\lambda_{ij}^m}{d_{pore}} \tag{C.1}$$

where d_{pore} is the characteristic pore diameter and λ_{ij}^m is the mean free path length of a molecule in a gas mixture. The mean free path length of a gas molecule is defined as the average distance traveled by a gas molecule between two intermolecular collisions in a pure gas. (Atkins and De Paula, 2006) However, since there is more than one species of gaseous species present, the mean free path length of a gas molecule needs to be corrected to take into account the presence of other gaseous species affecting the mean free path length of individual gas molecules. This correction has been derived by Schneider (Schneider, 1978) where the mean free path length of a gas molecule in a multicomponent gas mixture is expressed in Equation [C.2]).

$$\lambda_{ij}^m = \sum_{j=1}^{N} y_i \lambda_{ij} \tag{C.2}$$

λ_{ij} is the mean free path length of species i in species j and is defined in Equation [C.3].

$$\lambda_{ij} = \frac{RT}{pi\sigma_{ij}^2 N_A p_g}\sqrt{\frac{M_{ij}^*}{M_i}} \tag{C.3}$$

where M_i is the molecular weight of species i, N_A is Avogadro's number and p_g is the gas pressure, σ_{ij} is the averaged collision diameter of the species i in a gas mixture of species i and j and is expressed in Equation [C.4]

$$\sigma_{ij} = \frac{\sigma_i + \sigma_j}{2} \tag{C.4}$$

M_{ij}^* is the reduced molecular weight expressed in Equation [C.5]

$$\frac{1}{M_{ij}^*} = \frac{1}{M_i} + \frac{1}{M_j} \tag{C.5}$$

For Knudsen numbers, K_n below 0.1, bulk diffusion is dominant as the gas transport is in the continuum regime. For Knudsen numbers above 1, Knudsen diffusion is dominant. When $0.1 < K_n < 1$, both bulk diffusion and Knudsen diffusion are comparable in magnitude and the two parallel diffusion phenomena on mass transport must be included in the overall solution of the mass transport in porous media. The Knudsen diffusion coefficient, D_i^K for porous media is expressed in Equation [C.6].

$$D_i^K = \frac{2}{3}\frac{\phi_g}{\tau_g} r_{pore}\sqrt{\frac{8RT}{\pi M_i}} \tag{C.6}$$

To incorporate Knudsen diffusion in the multicomponent mass transport of porous media, we implement an averaged bosanquet binary diffusion coefficients (Equation [C.7]) that retains the cyclic symmetry of the Stefan-Maxwell diffusion coefficient and ensuring species mass conservation (Todd, 2003).

$$D_{ij}^{eff} = D_{ji}^{eff} = 0.5\frac{\phi_g}{\tau_g}\left(\frac{1}{1/D_i^K + 1/D_{ij}} + \frac{1}{1/D_j^K + 1/D_{ij}}\right) \tag{C.7}$$

Appendix D

Effective properties for composite electrodes

The effective properties for the composite electrode functional layer can be estimated by the widely adopted percolation and coordination-number theory that expresses the effective conductivities and active TPB length as a function of the composite electrode loading (Zhu and Kee, 2008). It is assumed that the electrode and electrolyte particles are spherical and the sintered particles overlap with a contact angle of θ. The TPB length per unit volume is determined by using Equation [D.1].

$$\lambda_{comp} = \ell_{ed-el} n_{tot} n_{ed} (1 - n_{ed}) Z_{ed-al} P_{ed} P_{el} \tag{D.1}$$

where ℓ_{ed-el} is the contact perimeter between the electrolyte particles and the electrode particles and is represented by $\ell_{ed-al} = 2\pi r sin\theta$. Z_{ed-el} is the average coordination number between the electrode and electrolyte particles defined by Equation [D.2] to Equation [D.4].

$$Z_{ed-el} = n_{el} \frac{Z_{ed} Z_{el}}{Z_{tot}} \tag{D.2}$$

$$Z_{ed} = 3 + \frac{(Z-3)\left(\frac{r_{el}}{r_{ed}}\right)^2}{n_{ed} + (1 - n_{ed})\left(\frac{r_{el}}{r_{ed}}\right)^2} \tag{D.3}$$

$$Z_{el} = 3 + \frac{(Z-3)}{n_{ed} + (1-n_{ed})\left(\frac{r_{el}}{r_{ed}}\right)^2} \tag{D.4}$$

where n_{ed} is the number fraction of the electrode, expressed as a function of solid phase volume fractions of the electrode and is defined by Equation [D.5].

$$n_{ed} = \frac{\phi_{ed}^v r_{ed}^3}{\phi_{ed}^v r_{ed}^3 + (1-\phi_{ed}^v) r_{el}^3} \tag{D.5}$$

r_{ed} is the electrode particle radius, r_{el} is the electrolyte particle radius, ϕ_{ed}^v is the electrode solid phase volume fraction, ϕ_{el}^v is the electrolyte solid phase volume fraction. P_{ed} and P_{el} is probability of the electrode and electrolyte particles to form a percolated network of its own phase from the dense electrolyte to the current collector respectively and it is expressed in Equation [D.6].

$$P_\alpha = \left[1 - \left(\frac{4.236 - Z_{\alpha\alpha}}{2.471}\right)^{2.5}\right]^{0.4} \tag{D.6}$$

where P_α represents either P_{ed} or P_{el}. n_{tot} is expressed in Equation [D.7].

$$n_{tot} = \frac{1-\phi_g}{(4/3)\pi[n_{ed} r_{ed}^3 + (1-n_{ed}) r_{el}^3]} \tag{D.7}$$

Effective conductivities of the electrode and electrolyte can be calculated using percolation theory, expressed in Equation [D.8].

$$\sigma_\alpha^{comp} = \sigma_\alpha^0 [(1-\phi_g)\phi_\alpha P_\alpha]^{2.5} \tag{D.8}$$

Appendix E

Supplemental calculations for inlet conditions

The mean inlet fuel and air velocities are calculated based on a target current density generation and 50% fuel and air utilization respectively. The target current density, i_{tar}, chosen is $2.5 \times 10^4 \frac{A}{cm^3}$. A high target current density was chosen to ensure that the anode is not limited by reactant supply. The amount of fuel (in mols) that will be consumed with the target current density, y_{fuel}, is calculated using Equation E.1

$$y_{fuel} = \frac{i_{tar} x_{ed} h_{ed}}{2F} \tag{E.1}$$

where $x_{ed} = 1cm$ is the length of the electrode and $h_{ed} = 550\mu m$ is the height of the electrode. Once y_{fuel} is calculated, the amount of H_2 (in mols) that needs to be fed to the anode, y^{in}_{H2}, considering the fuel utilization, U_{fuel} is calculated using Equation E.2

$$y^{in}_{H2} = \frac{y_{fuel}}{U_{fuel} x^{in}_{H2}} \tag{E.2}$$

The mean inlet fuel velocity is then calculated using Equation E.3

$$V_{fuel,inlet} = \frac{y^{in}_{H2} RT}{P h_{fuel}} \tag{E.3}$$

where $h_{fuel} = 1mm$ is the height of the fuel channel. A similar set of calculations is done to determine the mean inlet air velocities.